

Testing Convergence for Global Accretion Disks

John F. Hawley, Sherwood A. Richers, Xiaoyue Guan

*Department of Astronomy
University of Virginia
P.O. Box 400325
Charlottesville, VA 22904-4325*

`jh8h@virginia.edu; xg3z@virginia.edu`

and

Julian H. Krolik

*Department of Physics and Astronomy
Johns Hopkins University
Baltimore, MD 21218*

`jhk@pha.jhu.edu`

ABSTRACT

Global disk simulations provide a powerful tool for investigating accretion and the underlying magnetohydrodynamic turbulence driven by magneto-rotational instability (MRI). Using them to predict accurately quantities such as stress, accretion rate, and surface brightness profile requires that purely numerical effects, arising from both resolution and algorithm, be understood and controlled. We use the flux-conservative *Athena* code to conduct a series of experiments on disks having a variety of magnetic topologies to determine what constitutes adequate resolution. We develop and apply several resolution metrics: $\langle Q_z \rangle$ and $\langle Q_\phi \rangle$, the ratio of the grid zone size to the characteristic MRI wavelength, α_{mag} , the ratio of the Maxwell stress to the magnetic pressure, and $\langle B_R^2 \rangle / \langle B_\phi^2 \rangle$, the ratio of radial to toroidal magnetic field energy. For the initial conditions considered here, adequate resolution is characterized by $\langle Q_z \rangle \geq 15$, $\langle Q_\phi \rangle \geq 20$, $\alpha_{mag} \approx 0.45$, and $\langle B_R^2 \rangle / \langle B_\phi^2 \rangle \approx 0.2$. These values are associated with ≥ 35 zones per scaleheight H , a result consistent with shearing box simulations. Numerical algorithm is also important. Use of the HLLC flux solver or second-order interpolation can significantly degrade the effective resolution compared to the HLLD flux solver and third-order interpolation. Resolution at this standard can be achieved only with

large numbers of grid zones, arranged in a fashion that matches the symmetries of the problem and the scientific goals of the simulation. Without it, however, quantitative measures important to predictions of observables are subject to large systematic errors.

Subject headings: Black holes - magnetohydrodynamics (MHD) - stars:accretion
- methods: numerical

1. Introduction

Accretion is one of the fundamental power sources in astrophysical systems. Although the basic theory of accretion disks was formulated decades ago, it is not yet possible to carry out detailed modeling of accretion systems from first principles. The physics involved is too complex, and the problem is inherently multi-dimensional and time-dependent. The rapid increase in high performance computing capabilities has made possible increasingly detailed three-dimensional simulations, both in Newtonian (or pseudo-Newtonian) gravity and in the fully relativistic space-time of a Kerr black hole. The results of those simulations, however, require careful interpretation if they are to be usefully applied. The outcome of a given simulation depends not only on one's choices in physical properties, such as black hole spin and mass, and the density, temperature, and angular momentum of the accreting gas, but also on model-dependent factors such as the initial and boundary conditions, computational domain size, numerical resolution, and numerical algorithm. Of all these factors, those that are purely numerical can be the most vexing as their influences are both unintended and uncontrolled. One can be somewhat less concerned with the influence of numerical factors while conducting an initial *qualitative* survey of possible accretion behaviors and properties. But as we begin to answer more detailed *quantitative* questions that have the potential to relate more closely to observations, it becomes increasingly necessary to develop procedures to evaluate the merits of different simulations and the degree to which the numbers they provide can be regarded as accurate.

The accuracy of a given simulation is often described in terms of the *convergence* of the simulation. The terminology is imprecise, at least as it is often applied to accretion simulations. True numerical convergence means that the truncation errors in the solution are approaching zero at the rate consistent with the order of the scheme and that there are no remaining unresolved structures at the grid zone scale. In that case, a simulation result does not change as resolution is further increased. Formal convergence cannot be achieved for ideal magnetohydrodynamic (MHD), or hydrodynamic, simulations of turbulence that lack fixed viscous and resistive lengthscales; there will always be new structure created as

resolution is increased. Instead, what is usually meant by convergence in the context of such simulations is that physically important, macroscopic quantitative values (such as accretion rate and stress) do not change by a significant amount as the numerical resolution is increased (see also the discussion in Sorathia et al. 2012)

Even this less formal standard of convergence is hard to demonstrate or achieve in three-dimensional time-dependent simulations. First, it is generally impractical to employ ever-increasing resolution; one typically carries out simulations with as high a resolution as one can. Lower resolution simulations might provide useful data, but the interpretation may be ambiguous. If the best resolution one can achieve is still under-resolved, then the changes observed in lower resolution simulations may not be sufficient to determine how much more a simulation would change at ever higher resolution. The absence of a significant difference between a high and a lower resolution simulation is also not conclusive. If a simulation on a fine grid does not resolve an important process, neither will simulations done on a coarser grid.

Given these somewhat daunting practical difficulties, how can we judge the adequacy of a global accretion disk simulation? In accretion, the key dynamic quantity is the magnitude of the r - ϕ stress $\tau_{r\phi}$ that transports angular momentum outward through the disk. This is usually characterized in terms of the Shakura-Sunyaev (Shakura & Sunyaev 1973) parameter $\alpha = \tau_{r\phi}/P$, where P is the thermal pressure. Both the Maxwell and Reynolds stresses that make up $\tau_{r\phi}$ originate in MHD turbulence driven by the magneto-rotational instability (MRI; Balbus & Hawley 1991, 1992, 1998). Turbulence is notoriously difficult to compute adequately even in a local domain; the global problem is much more challenging. For accretion, the local domain is the “shearing box” (Hawley et al. 1995) which uses Cartesian geometry and includes the local tidal and Coriolis forces appropriate to differential rotation. There are two widely used versions of shearing box: stratified and unstratified, depending on whether or not they include the vertical component of gravity. The shearing box is characterized by an angular frequency Ω and the isothermal pressure scale height H . Different groups define H differently. Where it is necessary to distinguish usage, we label H as follows: for an isothermal sound speed c_s , $H_1 = c_s/\Omega$ and $H_2 = \sqrt{2}c_s/\Omega$. For the stratified shearing box H is the vertical scale height; in unstratified simulations it simply sets a characteristic scale based on the sound speed. Other important shearing box parameters include the box domain size, typically a few H in each dimension, and the initial magnetic field topology and strength, measured by $\beta = P_{gas}/P_{mag}$. Here again there is variation in how β is defined, e.g. in terms of average values or values at the equatorial plane.

The local nature of the shearing box makes it possible to use a large number of grid zones per H . Some recent shearing box models used 32–128 zones per H_2 in Davis et al. (2010),

32–144 zones per H_2 in Simon et al. (2012), and 12.8 zones per H_1 in Guan & Gammie (2011). These local simulations find $\alpha \sim 0.01$ – 0.1 ; Simon et al. (2012), found $\alpha \approx 0.02$ – 0.03 to be typical, with considerable temporal and spatial variation, while the less well-resolved simulations of Guan & Gammie (2011) report $\alpha = 0.01$ – 0.02 . Work continues in the local box models to better understand resolution effects, as well as the impacts of non-zero resistivity and viscosity (Fromang et al. 2007; Lesur & Longaretti 2007; Simon & Hawley 2009).

It is hoped that the insights gained from studies of MRI-driven turbulence in local models will carry over to the global domain. To establish that this is so, we need first to determine whether the local shearing box is representative of the local behavior within a global disk. Since the MRI is a local instability, it seems reasonable to assume that the properties of turbulence observed in the shearing box are applicable in global contexts. The recent work of Simon et al. (2012) on large shearing boxes suggests that this is the case for some properties of the turbulence (e.g. α), but that there are also what they refer to as “mesoscale” structures on scales $\sim 10H$. On the other hand, when shearing-boxes are sufficiently large, the curvature of real disks may become important.

Next, what resolutions do global simulations require, and can shearing box results be used to determine this? Because accretion disks span large radial distances and are thin, $H/R < 1$, it is extremely difficult for global models to achieve anything close to the resolution used in local simulations. The approach taken by Hawley et al. (2011) was to characterize the resolution-dependence of certain average properties of MRI-driven turbulence in well-resolved local shearing box simulations. Characteristic properties that approach a fixed value as resolution increases then become diagnostics of quality and can be used as a standard against which global simulations can be evaluated. Based on comparisons to well resolved shearing box simulations, Hawley et al. (2011) concluded that no global simulations have yet been run with sufficient resolution as to be deemed “converged” in certain essential MHD properties.

The first of these diagnostics derives from the characteristic wavelength of the MRI mode, $\lambda_{MRI} = 2\pi v_a/\Omega$, where v_a is the Alfvén speed; λ_{MRI} is the distance an Alfvén wave travels in one orbit. This definition differs from the precise fastest growing wavelength by a factor close to unity. From this definition Hawley et al. (2011) define two simulation quality metrics from the ratio of this length to the grid zone size, namely

$$Q_z = \frac{\lambda_{MRI}}{\Delta z} = \frac{2\pi|v_{az}|}{\Omega\Delta z}, \quad (1)$$

where v_{az} is the z component of the Alfvén speed, and

$$Q_\phi = \frac{\lambda_{MRI}}{R\Delta\phi} = \frac{2\pi|v_{a\phi}|}{R\Omega\Delta\phi} = \frac{2\pi H_2}{(\beta_\phi^{1/2} R\Delta\phi)}, \quad (2)$$

which usefully defines Q_ϕ in terms of the local scale height H and β_ϕ , the ratio of the gas to magnetic pressure including only the contribution from the toroidal field. The importance of resolving the characteristic MRI wavelength has long been recognized. Previous numerical tests (e.g., Hawley & Stone 1995; Sano et al. 2004; Fromang & Nelson 2006) indicate that obtaining proper *linear* growth rates for the fastest-growing MRI modes requires > 6 zones per wavelength. Flock et al. (2010) carried out a study of the linear MRI in a global disk configuration and concluded that $Q_z > 8$ was required to accurately capture the growth rates, at least for numerical schemes that were relatively low in numerical diffusion. Although the Q parameters were invented to calibrate the description of linear amplitude MRI, they continue to be useful diagnostics for assessing the resulting fully nonlinear turbulence. The empirical results of Hawley et al. (2011) suggest that in the nonlinear regime $Q_\phi \gtrsim 20$ and $Q_z \gtrsim 10$ are minimum values to describe MRI-driven turbulence.

Shearing box results show that fully developed MRI turbulence has certain average magnetic properties that also can be used as diagnostics. Hawley et al. (2011) examined two such diagnostics, the ratio of the Maxwell stress to the magnetic pressure, $\alpha_{mag} = M_{R\phi}/P_{mag}$, and the ratio of the radial to toroidal magnetic energy, B_R^2/B_ϕ^2 . When suitably averaged over the computational domain (as indicated by angle brackets, e.g., $\langle B_R^2 \rangle / \langle B_\phi^2 \rangle$) these quantities appear to approach specific values for well-resolved simulations. The earliest shearing box simulations (Hawley et al. 1995) found that α_{mag} is nearly constant from simulation to simulation. Blackman et al. (2008) arrived at a similar conclusion across a large sample of published unstratified shearing box results. Hawley et al. (2011) found that $\langle B_R^2 \rangle / \langle B_\phi^2 \rangle$ increases with $\langle Q_z \rangle$ and seems to approach a value of ~ 0.2 at high $\langle Q_z \rangle$. Although $\langle B_R^2 \rangle / \langle B_\phi^2 \rangle$ is related to α_{mag} , they are not equivalent; α_{mag} measures the correlation between B_R and B_ϕ , whereas $\langle B_R^2 \rangle / \langle B_\phi^2 \rangle$ is a ratio of average energies, with no dependence on correlations between the two components.

Halfway between the global disk and the shearing box is the *cylindrical disk*, i.e., global models that do not include the vertical component of gravity. These are viewed as a model of the equatorial region of a disk on scales less than H . A study undertaken by Sorathia et al. (2012) computed a set of cylindrical disk models using the *Athena* code, which has recently been extended to cylindrical coordinates (Skinner & Ostriker 2010). Sorathia et al. (2012) studied three different initial field topologies: sinusoidally varying vertical field, net vertical field and net toroidal field. They achieved very high resolution, consistent with well-resolved shearing boxes, by restricting the radial and vertical domain in the problem. They also used a numerical technique called “orbital advection” that takes into account the background orbital motion by locally boosting into a co-rotating frame. This removes the orbital motion from the Courant limit, increasing the timestep size. This step may also reduce the numerical diffusion that would arise from advection through the grid due to the orbital motion.

Their fiducial grid has a radial domain from $[1, 4]$, a vertical domain $[-0.4, 0.4]$ and a full 2π ϕ domain, spanned by $480 \times 1920 \times 128$ zones for $\Delta R = \Delta z = 2\Delta\phi = 6.25 \times 10^{-3}$. The sound speed is set so that the vertical domain is 4 isothermal scaleheights at $R = 2$, giving a resolution of 32 zones per H_2 . From these simulations they conclude that the most important indicator of well-resolved MRI-driven turbulence, regardless of initial magnetic field topology or strength, is the magnetic tilt angle, $\theta_B = \arcsin(\alpha_{mag})/2 \approx 13^\circ$ (Guan & Gammie 2009); this corresponds to $\alpha_{mag} \approx 0.44$. They further stress the importance of an effective resolution of $H/\Delta z > 32$, the use of comparable grid zone size in all three dimensions, and the importance of azimuthal resolution, recommending $R\Delta\phi \leq 2\Delta z$. They found, as suggested by Hawley et al. (2011), that higher Q_ϕ values (≥ 25) can compensate for lower Q_z values, while $Q_z \geq 10$ –15 can compensate for $Q_\phi \approx 10$.

The purpose of the present work is to extend these local-to-global investigations using a systematic study of resolutions in full global simulations. We will test whether the diagnostics developed to date continue to measure a simulation’s quality, and attempt to bring a global model toward adequate resolution. We will compare different initial magnetic field topologies and strengths and, since numerical accuracy is not solely a question of grid zones, also some simple variations in the numerical algorithm.

In §2 of this paper we present the numerical model we will examine and discuss some diagnostic measures. §3 presents a resolution study for one specific fiducial initial magnetic field configuration. In §4 we examine variations on both this base model and on the algorithmic choices made within the *Athena* code. Discussion and conclusions are presented in §5.

2. Numerics and Diagnostics

The simulations in this paper are all carried out using the *Athena* code (Stone et al. 2008) using version 4.1 which incorporates cylindrical coordinates, (R, z, ϕ) , as developed by Skinner & Ostriker (2010). *Athena* solves the equations of MHD in conservative form (mass, momentum, total energy and magnetic flux) using a flux-conservative scheme. The principal components of *Athena* include the overall integration scheme, the reconstruction algorithm within a zone, and the flux solver. Except where noted, we use the directionally unsplit CTU integrator of Colella (1990), third-order piece-wise parabolic reconstructions (Colella & Woodward 1984), and the HLLD flux solver of Miyoshi & Kusano (2005).

Since the aim of this study is to explore convergence in global simulations, and high resolution is more easily attained by limiting the domain size and evolution time required,

we choose to study a region that is close to the black hole. The initial condition is based on the GT4 torus from Hawley (2000) which was subsequently studied using a pseudo-Newtonian potential, $\propto 1/(r - r_g)$, by Hawley & Krolik (2001). That previous work used units in which $r_g = 1$, and here we use units with $r_g = 2M$. This places the innermost stable circular orbit (ISCO) of the pseudo-Newtonian potential at $6M$. The computational domain is a cylindrical annulus running from $R = 4M$ to $R = 44M$ and from $-15M$ to $15M$ in z . The ϕ domain spans $\pi/2$ in radians; the size of the ϕ domain can influence the outcome of a simulation (Beckwith et al. 2011; Flock et al. 2012), but for the present study we hold that fixed. We place outflow conditions on the R and z boundaries and periodic boundary conditions in the ϕ direction. The outflow boundary condition is the same as used in Sorathia et al. (2012). There are four halo, or “ghost” zones at each boundary and these are given the same conserved state values as the last physical zone on the grid. If a momentum vector is directed into the grid, it is reset to zero and the total energy adjusted appropriately.

The initial torus has a pressure maximum at $R = 20M$ and an inner boundary at $R_{in} = 11M$, with an angular momentum distribution parameter $q = 1.68$, where $\Omega \propto R^{-q}$. The closer the angular momentum distribution is to Keplerian ($q = 1.5$), the thinner the initial torus will be. We use an adiabatic equation of state, $P = K\rho^\Gamma$ with $\Gamma = 5/3$, and $K = 0.0034$. Rather than using a scale height based on the isothermal sound speed, we use the density scale height,

$$H = \frac{\int \rho |z| dz}{\int \rho dz}, \quad (3)$$

as a measure of disk thickness. Using this, the initial thickness of the torus at the pressure maximum is $H/R = 0.07$. This definition of H results in a smaller value than would be obtained by using the sound speed at the equator; H_2 would be larger by 1.9, for example. In the absence of additional physics such as a cooling function or self-gravity, the density units are arbitrary and set by the choice of K . The initial total mass is 788 in code units (assuming a domain that spans the full 2π in ϕ). For the pseudo-Newtonian potential the Keplerian frequency is $\Omega = (R^{1/2}[R - 2])^{-1}$, giving an orbital period at the ISCO of $61.5M$ and $506M$ at the torus pressure maximum. The initial torus is seeded with random pressure fluctuations at the 1% level.

The torus contains a weak (subthermal) initial magnetic field. In Hawley & Krolik (2001), the initial magnetic is a nested dipolar loop configuration (referred to here as a “one-loop” configuration) where the vector potential is set to be $A_\phi = C(\rho - \rho_{cut})$, with $\rho_{cut} = 0.25\rho_{max}$, the maximum density at the pressure maximum. An alternative field topology consists of two loops generated by toroidal currents of different signs (the “two-

loop” configuration). For this we use the the vector potential function of Shafee et al. (2008),

$$A_\phi = C [(\rho - \rho_{cut})r^{0.75}/\rho_{max}]^2 \sin [\ln(r/S)/T] \quad (4)$$

where r is the spherical coordinate radius, ρ_{cut} is set at 20% of the density maximum (thus confining the initial field to well within the edge of the initial torus), $S = 1.1 R_{in}$, and $T = 0.16$.

The vector potential establishes the field geometry and the relative strength of the field components throughout the torus, but the overall field strength can be set by whatever normalization is desired. The main requirement is that the field should have resolved MRI wavelengths that fit within the torus. We normalize the the initial magnetic field strength using an average plasma β value, $2\langle P \rangle / \langle B^2 \rangle$. Several initial β values will be examined. We will find, however, that a very useful way to characterize the field strength is with reference to the initial quality factors, e.g. Q_z . This immediately indicates the field strength relative to the grid resolution within the torus, facilitating comparisons of quite different simulations.

Using the results of Hawley et al. (2011) we can estimate the number of grid cells required to achieve certain values of the Q parameters in the evolving torus. For the vertical direction the number of cells per H is estimated to be

$$N_z \simeq 16 (\beta/100)^{1/2} (\langle v_A^2 \rangle / \langle v_{Az}^2 \rangle)^{1/2} (Q_z/10) \quad (5)$$

where the ratio of the Alfvén speeds reflects the fraction of the total magnetic energy in the vertical component alone, typically ~ 0.01 – 0.1 . Assuming that $\beta \sim 10$ in the turbulent phase, and that the vertical field energy will be ~ 0.05 of the total magnetic energy, condition (5) requires 21 vertical grid zones per H .

Adequate resolution of the toroidal MRI in a full 2π simulation is estimated to require

$$N_\phi \simeq 1000 (0.1 R/H) (\beta/100)^{1/2} (Q_\phi/10) \quad (6)$$

azimuthal cells. Again, assuming $\beta \sim 10$ and $H/R \sim 0.2$ (the simulated torus will thicken due to disk heating), the Q_ϕ condition requires 75 ϕ grid zones in a $\pi/2$ domain. At the pressure maximum ($R = 20M$) this requires $\Delta z \simeq 0.2$ and $\Delta\phi = 0.021$ (corresponding to $R\Delta\phi = 0.42$ at the pressure maximum). A representative grid resolution would then be $\sim 210 \times 75 \times 160$ zones in (R, ϕ, z) , not too-large a number. On a cylindrical grid, however, assuming a constant H/R , the resolution requirement on Δz increases as R decreases. A $\Delta z = 0.06$ is required to satisfy the Q_z criterion at the ISCO location of $R = 6M$, which would increase the required number of vertical zones to 500. Since the proposed condition on the radial grid is simply that the cell aspect ratio be on order unity, a comparable number of R zones will be used.

To analyze the simulations, data is output once every ISCO orbital period ($= 61.5M$). To obtain a rough overall measure of a simulation’s evolution, global totals such as mass, total energy, and components of the magnetic and kinetic energies are computed every tenth of an orbit at the ISCO. Integrations over radial shells give azimuthally and vertically averaged values at each radius. For example, the mass in a radial shell is

$$m(R) = \int \rho R d\phi dz, \quad (7)$$

and the accretion rate is

$$\dot{M}(R) = \int \rho v_R R d\phi dz. \quad (8)$$

Since the focus is on the properties of the disk itself, most averages will be density-weighted. For example, Q_ϕ and Q_z are intended to measure the functioning of the MRI-driven turbulence within the disk, not in the corona where the Alfvén speeds are much higher. Thus they are computed as a function of radius using

$$\langle Q_z \rangle(R) = \frac{\int Q_z \rho R d\phi dz}{\int \rho R d\phi dz}. \quad (9)$$

On a more mundane note, the choice of grid resolution is also influenced by the requirements of parallel domain decomposition, the number of computational nodes available in a system, and the number of cores per node. The highest resolution simulations were run on the *Kraken* system at the National Institute for Computational Science (NICS) which has 12 cores per node. For *Kraken*, maximum efficiency requires use of domain decomposition in multiples of 12, whereas powers of two were best for the University of Virginia Astronomy Department’s *Hyades* cluster, which was used for the lower resolution simulations.

3. Resolution Study

In the present study we choose one simulation to be the “fiducial simulation” and vary the conditions, both physical and numerical, relative to that benchmark. Here, the designated fiducial simulation uses an evenly spaced grid of $256 \times 64 \times 252$ zones, with $\Delta R = 0.156$, $\Delta z = 0.117$ and $\Delta\phi = .025$. By the Q criteria (5), this resolution should produce a turbulent disk that has Q values close to, but just below, the thresholds of $\langle Q_z \rangle = 10$ and $\langle Q_\phi \rangle = 20$. For a resolution test we double and halve the size of the R and z zones compared to the fiducial grid. The models are labeled Twoloop-128 for the $128 \times 64 \times 128$ grid, Twoloop-256 for the fiducial $256 \times 64 \times 256$ grid, and Twoloop-512 for the $512 \times 120 \times 512$ grid. These are run to $\sim 10^4 M$ in time, or about 160 ISCO orbits. Although this might seem

to be a limited evolution time (and in some respects it is), it is nevertheless sufficient for most of the mass to be lost off the grid. (For comparison, the simulation of Hawley & Krolik (2001) ran to only $3000M$ in time.) The fiducial simulation uses the two-loop initial field configuration with an average initial magnetic field strength $\beta = 1000$. For the two-loop configuration there are three regions of significant initial vertical field: near the disk inner edge, at the pressure maximum, and at the disk outer edge. These regions have maximum initial $\langle Q_z \rangle$ values at the equator, reaching 3, 6, and 5.5 for the Twoloop-256 model; the other two resolutions have twice or half those values.

We list these three simulations and all the subsequent variations (considered in §4) in Table 1. In addition to the two-loop model run at three resolutions, we run a set of two-loop models with the same grid as the fiducial run, but different initial field strength. We also consider the fiducial run with algorithmic variations: an alternate flux solver and second-order zone reconstruction. Next we carry out simulations with alternative initial field topologies: the dipolar loop configuration (one-loop) and a toroidal initial field. Several resolutions are used for these alternative field topologies. The table lists the number of grid zones and the grid zone sizes for these simulations; since *Athena* currently does not allow for variable grid zone size, this is fixed across the domain. Any key property of the simulation is noted in the column labeled “Comment.” The number of vertical zones per scale height, $H/\Delta z$ is measured at the initial pressure maximum, where $H/R = 0.07$, and is given for reference. By the standards of shearing box simulations, the zones per scaleheight numbers are all low, but because H increases as the disk heats, this number will increase with time.

An overall sense of the evolution in the two-loop models is given by the total mass on the grid, whose history is shown in Figure 1. Each simulation shows a different pattern in the development of the accretion rate, making detailed comparisons between the simulations difficult. Moreover, in all cases the initial condition is a torus of finite mass. There can be no ultimate long-term steady state in which averaged properties can be defined because the mass on the grid steadily diminishes; indeed, in all these simulations, the mass at the end of the simulation is significantly less than at the beginning. This fact creates another problem of comparison if one wishes to set these results beside those of shearing box simulations, whose typical durations are hundreds of orbits. For example, Simon et al. (2012) regard the first 50 orbits of their shearing box simulations as the “transient” phase. Here 50 orbits at the ISCO is $3000M$, and by that point approximately 10% of the initial torus mass is gone.

The evolution of all our simulations is qualitatively similar to what was seen in Hawley & Krolik (2001). A brief initial linear MRI growth phase leads to turbulence throughout the disk, followed by an extended period of evolution characterized by the steady decline in mass owing to accretion and outward mass flow. In Figure 1a the dashed lines indicate the fraction of

Table 1. Simulation List

Name	(R, ϕ, z)	ΔR	$\Delta \phi$	Δz	$H/\Delta z$	Comment
Twoloop-128	$128 \times 64 \times 128$	0.313	0.0245	0.234	6	$\beta = 1000$
Twoloop-256	$256 \times 64 \times 256$	0.156	0.0245	0.117	13	Fiducial
Twoloop-512	$512 \times 120 \times 512$	0.078	0.0131	0.059	25	
Twoloop-256w	$256 \times 64 \times 256$	0.156	0.0245	0.117	13	$\beta = 4000$
Twoloop-256l	$256 \times 64 \times 256$	0.156	0.0245	0.117	13	$\beta = 500$
Twoloop-256b	$256 \times 64 \times 256$	0.156	0.0245	0.117	13	$\beta = 250$
Twoloop-256e	$256 \times 64 \times 256$	0.156	0.0245	0.117	13	HLLE
Twoloop-256s	$256 \times 64 \times 256$	0.156	0.0245	0.117	13	2nd Order
Oneloop-128	$128 \times 64 \times 128$	0.313	0.0245	0.234	6	$\beta = 1000$
Oneloop-256	$256 \times 64 \times 256$	0.156	0.0245	0.117	13	
Oneloop-512	$512 \times 120 \times 512$	0.078	0.0131	0.059	25	
Oneloop-320b	$320 \times 120 \times 240$	0.125	0.0131	0.125	10	$\beta = 100$
Toroidal-64	$128 \times 64 \times 128$	0.313	0.0246	0.234	6	$\beta_\phi = 10$
Toroidal-128	$128 \times 128 \times 128$	0.313	0.0123	0.234	6	
Toroidal-192	$256 \times 128 \times 192$	0.156	0.0123	0.156	9	
Toroidal-128s	$128 \times 128 \times 128$	0.313	0.0123	0.234	6	2nd Order
Toroidal-128w	$128 \times 128 \times 128$	0.313	0.0123	0.234	6	$\beta_\phi = 100$
Twoloop-512t	$512 \times 128 \times 512$	0.078	0.0123	0.059	25	$\beta = 1000$
Twoloop-256t	$256 \times 64 \times 256$	0.156	0.0245	0.117	–	re-grid
Twoloop-128t	$128 \times 32 \times 128$	0.313	0.0490	0.234	–	$t = 4600M$

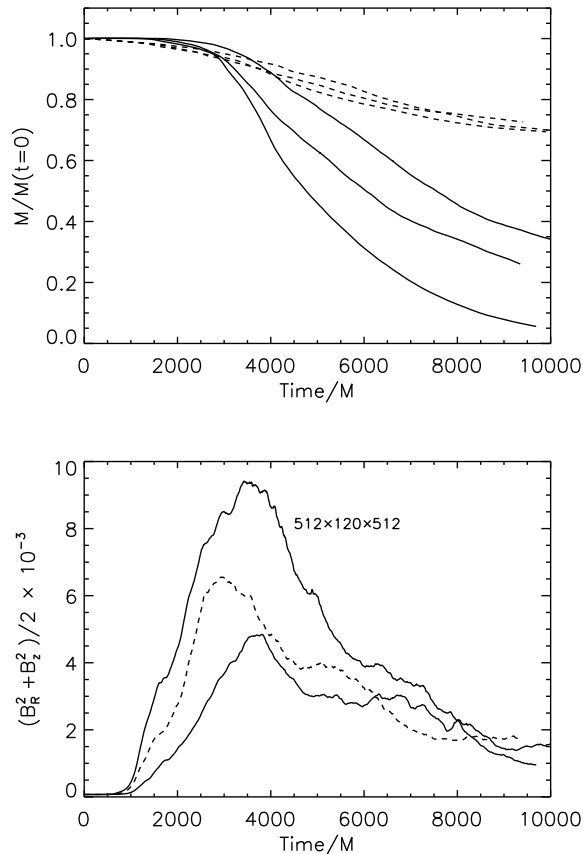


Fig. 1.— (a) The total mass on the grid (solid lines) and the accumulated mass accreted through the inner radial boundary (dashed lines) as a function of time. The $512 \times 120 \times 512$ model (labeled) loses the most mass followed by the $256 \times 64 \times 256$ model and finally the $128 \times 64 \times 128$ model. The same ordering holds for mass accreted, although the differences are not as large. (b) Time evolution of the poloidal field energy on the grid for two-loop simulations of different resolution. The $512 \times 120 \times 512$ model is labeled, the dashed line is the $256 \times 64 \times 256$ model, and the remaining line is the $128 \times 64 \times 128$ model.

the mass lost through the inner radial boundary. The majority of the mass leaves through the outer boundary. By time $10^4 M$ in Twolooop-512, 31% of the initial mass has accreted, 61% of the initial mass has left through the outer radial boundary, 6% remains on the grid and a small additional amount has left through the z boundaries. Net inflow occurs primarily inside of a point just outside the initial disk pressure maximum. The location of P_{max} moves to $R \approx 16M$ after $t = 3000M$. The accretion time at the initial pressure maximum can be estimated as $\sim R/\langle v_R \rangle \sim 2 \times 10^4 M$, but the actual accretion time is much shorter. Initially only 18% of the mass is located inside the pressure maximum, and by the end of the simulation 31% of the total mass has accreted, hence some of the mass from outside of the initial torus pressure maximum has, in fact, accreted. The plot shows that similar mass fractions accrete in the Twolooop-128 and Twolooop-256 run; indeed, for this quantity the major difference between the different resolutions is the amount of mass lost through the outer boundary. As observed in Hawley et al. (2011) and emphasized in Sorathia et al. (2012), the rate of accretion is more rapid than would be inferred from a simple estimate based on the average α value and the radius of the initial torus pressure maximum; matter from the initial torus quickly fills the inner disk as orbital shear creates strong magnetic stress in the relatively concentrated field near its inner edge.

Figure 1b shows the evolution of the total poloidal field energy as a function of time. There are clear differences due to resolution in the linear growth of the poloidal magnetic field. The higher the resolution, the earlier and the faster the poloidal field energy increases, and the larger it becomes. Because MRI growth rates are proportional to Ω , field growth occurs at different rates throughout the torus. The inner part of the disk evolves first, with turbulence developing by $t = 1000M$, followed by the center of the disk by $t = 1500M$, and throughout the whole disk by $t = 2500M$. This greater poloidal field energy corresponds directly to the larger stress and mass accretion rates found in Twolooop-512 through $t = 4000M$. Beyond that point the total field energy declines for all resolutions as mass and field leave the grid. This decline does not mean a reduction in magnetization or a decay of the turbulence, however. It is due to field lost off the grid along with the mass. The poloidal field energy per unit mass (Figure 1b divided by Figure 1a) remains relatively flat with time for the two lower resolution runs, and increases with time for the highest resolution model.

The initial growth of the toroidal field energy, B_ϕ^2 , is much less dependent on resolution; it grows at the same rate for all three simulations. Toroidal field amplification occurs mainly through azimuthal shear acting on the (initial) radial field, and this effect is easily captured at even modest resolution. The peak toroidal field energy value increases with resolution, however. Beyond $t = 4000M$ the toroidal field energy per unit mass remains nearly constant for all three models, but for Twolooop-512 this value is twice what it is in the lower resolution simulations.

We see that the overall evolution of the torus with time complicates the interpretation of a number like mass accretion rate or field strength. In Figure 2 we compute the accretion rate at time t as a fraction of the mass remaining on the grid at that time. When normalized in this manner, the highest resolution simulation stands out as maintaining a robust accretion rate relative to the available mass.

Figure 3 shows the three resolutions at $t = 4920M$, when the inner disk is accreting at a roughly constant rate. The density plot (left column) shows how increased turbulence and accretion have greatly reduced the total mass in the highest resolution simulation compared to the lowest. The radial field plot (right column) suggests that the larger scale fields are comparable from one resolution to the next, but increased resolution brings stronger fields on small scales and much more structure.

Table 2 gives diagnostic quantities for these runs, time-averaged between $t = 4000$ – $6150M$, corresponding to the time after the initial energy peak (Fig. 1). The accretion rates are given both relative to the initial torus mass, $\dot{M}/M(t = 0)$, and to the current total mass, \dot{M}/M . As suggested by Figure 1, the time-averaged \dot{M} appears somewhat insensitive to resolution, at least for this time period. An examination of accretion as a function of time finds that as resolution is increased, accretion begins earlier and rises to higher initial values, but after roughly $t \sim 5000M$ the lower resolution models have higher $\dot{M}(t)$. The reason is that the mass density is higher at late time in the low resolution simulations; more of the torus mass remains to be accreted. The value of \dot{M}/M , however, shows a systematic increase with resolution.

The other Table 2 values are density-weighted averages on radial shells. For each diagnostic, two numbers are listed corresponding to the value at the ISCO and at $R = 20M$. Because the grid is cylindrical, the number of z zones per H will decrease inward for any disk with a constant H/R . $\langle Q_z \rangle$ declines inward with radius at a rate that is very nearly proportional to R . This means that the vertical Alfvén speed v_{az} increases inward as $R^{-1/2}$ (eq. 1). $\langle Q_z \rangle$ also increases slowly with time in the inner part of the disk; the Alfvén speed increases with decreasing density as the evolution proceeds. A strong resolution effect is apparent: as resolution decreases, $\langle Q_z \rangle$ is reduced by more than can be accounted for simply by the increase in Δz .

The value of $\langle Q_\phi \rangle$ shows less dependence on R , but resolution does influence its value. The Twolooop-128 and Twolooop-256 models have the same ϕ grid, so the increase in $\langle Q_\phi \rangle$ from Twolooop-128 to Twolooop-256 is due to the improved poloidal resolution. The Twolooop-512 model increases the number of ϕ zones to 120, and the increase in $\langle Q_\phi \rangle$ is more than can be attributed to the decrease in $\Delta\phi$. Average magnetic field strengths increase with resolution.

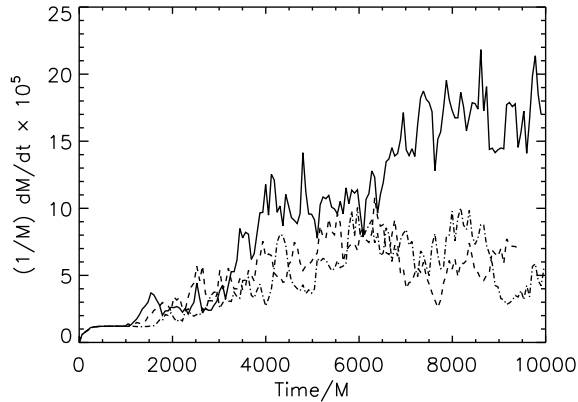


Fig. 2.— Accretion rate divided by mass remaining on grid, \dot{M}/M as a function of time. The solid line is the $512 \times 120 \times 512$ model, the dashed line the $256 \times 64 \times 256$ model and the dot-dashed line is $128 \times 64 \times 128$ model.

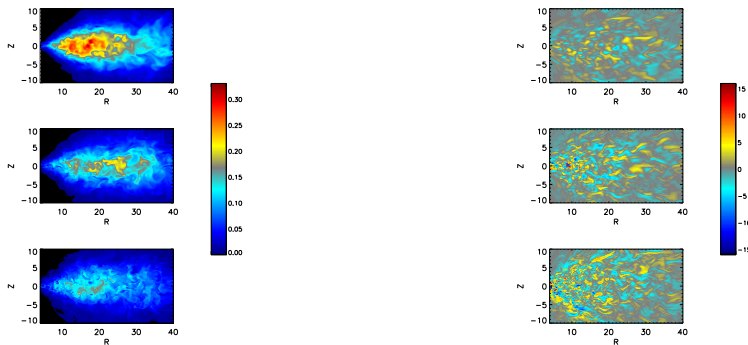


Fig. 3.— (a) Density and (b) radial magnetic field for the initial two loop simulations with three resolutions: From top to bottom, Twoloop-128, Twoloop-256, Twoloop-512. The images show a single slice through the flow along the $\phi = 0$ plane, at $t = 4920M$. The density is in units of the initial maximum density in the torus, and the magnetic field is in units of the initial maximum radial field strength.

Table 2. Simulation Results

Name	$\dot{M} \times 10^5$	$\dot{M}/M \times 10^5$	α_{mag}	$\langle Q_z \rangle$	$\langle Q_\phi \rangle$	$\langle B_R^2 \rangle / \langle B_\phi^2 \rangle$	$\langle \beta \rangle$	H/R	stress $\times 10^{-6}$
Twoloop-512	4.8	10.2	0.54–0.45	13–36	39–31	0.19–0.20	7.5–13	0.22–0.18	2.6–0.52
Twoloop-256	4.2	6.8	0.50–0.46	4.5–15	19–16	0.13–0.18	8.1–13	0.20–0.18	2.0–0.57
Twoloop-128	4.5	5.9	0.34–0.40	1.1–5.1	16–13	0.05–0.11	11–18	0.16–0.16	1.3–0.50
Twoloop-256w	2.7	3.1	0.46–0.41	3.7–8.4	17–10	0.10–0.12	10.1–19	0.17–0.13	1.1–0.47
Twoloop-256	4.2	6.8	0.50–0.46	4.5–15	19–16	0.13–0.18	8.1–13	0.20–0.18	2.0–0.57
Twoloop-256l	4.7	10.0	0.50–0.42	5.3–16	22–17	0.13–0.16	7.6–13	0.22–0.18	2.2–0.43
Twoloop-256b	3.6	13.4	0.56–0.44	9.2–26	30–22	0.19–0.20	4.7–10	0.31–0.23	2.5–0.38
Twoloop-256e	4.3	5.9	0.39–0.42	3.3–12	17–14	0.07–0.12	11–17	0.17–0.16	1.4–0.53
Twoloop-256s	5.6	7.8	0.43–0.39	3.4–13	19–17	0.08–0.11	8.1–14	0.18–0.17	2.5–0.52
Oneloop-128	3.2	3.9	0.33–0.38	1.0–4.5	14–13	0.05–0.09	16–14	0.16–0.13	0.94–0.33
Oneloop-256	2.5	3.3	0.46–0.40	3.3–7.8	15–9.3	0.10–0.11	11–25	0.18–0.13	0.87–0.23
Oneloop-512	2.6	3.7	0.52–0.43	8.1–22	28–21	0.17–0.17	9.7–18	0.19–0.15	1.20–0.43
Oneloop-320b	2.8	12.4	0.53–0.44	6–22	42–41	0.16–0.18	7.7–8.5	0.25–0.20	1.3–0.36
Toroidal-64	2.6	4.1	0.27–0.34	1.0–2.8	14–10	0.04–0.07	17–29	0.16–0.14	0.62–0.25
Toroidal-128	3.1	1.1	0.38–0.42	1.4–7.1	33–32	0.07–0.13	13–15	0.20–0.19	0.82–0.34
Toroidal-192	2.6	4.8	0.47–0.44	2.4–9.2	30–24	0.11–0.15	12–26	0.20–0.19	0.86–0.24
Toroidal-128s	1.7	2.1	0.17–0.27	1.0–2.5	37–23	0.02–0.04	10–17	0.18–0.13	0.43–0.36
Toroidal-128w	2.3	5.0	0.33–0.39	1.2–4.3	28–23	0.05–0.10	17–25	0.18–0.16	0.52–0.23
Twoloop-512t	4.0	8.0	0.53–0.45	12–36	40–31	0.18–0.21	7.5–14	0.21–0.20	2.2–0.50
Twoloop-256t	5.8	7.4	0.51–0.45	4.4–14	19–14	0.14–0.18	8.2–20	0.21–0.20	1.6–0.34
Twoloop-128t	6.3	7.6	0.38–0.39	1.0–5.0	6.9–6.0	0.06–0.11	18–27	0.18–0.20	0.88–0.23

The ratio of field energies, $\langle B_R^2 \rangle / \langle B_\phi^2 \rangle$, also increases with resolution, again, particularly near the ISCO. Figure 4 examines the relation between $\langle Q_z \rangle$ and $\langle B_R^2 \rangle / \langle B_\phi^2 \rangle$ by plotting the values computed for individual radial shells for each radial grid zone between $R = 6\text{--}20M$, and for all individual data files between $t = 4000M$ and $6150M$. The three resolutions sort themselves into distinct regions of the graph with the value of $\langle B_R^2 \rangle / \langle B_\phi^2 \rangle$ rising with increasing $\langle Q_z \rangle$ until $Q_z \approx 15$. Within a given simulation, lower $\langle Q_z \rangle$ values tend to correspond to smaller R ; the spread of points represents the inherent variability. This figure improves upon Figure 14 of Hawley et al. (2011), where it was noted that $\langle B_R^2 \rangle / \langle B_\phi^2 \rangle$ appeared to be leveling off near a value of 0.2, but there were insufficient points with high enough $\langle Q_z \rangle$ to make that observation as conclusive as it is here. Figure 5 shows the time evolution of $\langle B_R^2 \rangle / \langle B_\phi^2 \rangle$ averaged between $R = 6$ and $20M$ for the three runs. Throughout the evolution, the values of $\langle B_R^2 \rangle / \langle B_\phi^2 \rangle$ remain distinct among the three resolutions. A very similar behavior was seen in the shearing box simulations, shown in Figure 4 of Hawley et al. (2011).

Resolution also affects the value of α_{mag} , although not as dramatically. For example, $\alpha_{mag} \sim 0.45$ for both the Twolooop-256 and 512 runs at $R = 20M$. Figure 6 plots individual α_{mag} values for the three runs for all radii between $10\text{--}20M$ and for times from $t = 4000$ to $6150M$, and Figure 7 plots $\langle B_R^2 \rangle / \langle B_\phi^2 \rangle$ in the same way. The data were restricted to this radial range to avoid the region near the ISCO where both quantities tend to increase owing to the transition from turbulence to streaming inflow. The three different resolutions separate nicely into distinct regions due to two reasons: increased resolution halves the size of Δz , and the stronger magnetization in higher resolution leads to greater heating and increased H . From the first of these plots we see that α_{mag} is relatively constant (albeit with significant variation) with an average value ~ 0.45 for resolutions greater than 20 zones per H . Twolooop-128 exhibits a decrease in α_{mag} as the number of zones drops below this value. The plot shows that $\langle B_R^2 \rangle / \langle B_\phi^2 \rangle$ increases with resolution until leveling off at a value $\simeq 0.2$ when there are roughly 35 zones per H . This comparison suggests that while both of these quantities are good indicators of resolution, the $\langle B_R^2 \rangle / \langle B_\phi^2 \rangle$ criterion is the more demanding.

At intermediate resolutions there is a general trend of increasing α_{mag} with $\langle B_R^2 \rangle / \langle B_\phi^2 \rangle$. At high resolution, B_r^2 and B_ϕ^2 become proportional across a wide range of values. At lower resolution, there is still a general proportionality, but B_ϕ^2 tends to be larger for a given value of radial field energy. Lower resolution results in less effective generation of poloidal field, although what radial field there is remains correlated with B_ϕ .

The density-weighted value of β , time-averaged between $t = 4000\text{--}6150M$ shows an increase in relative magnetization with resolution. Figure 8 plots the radial dependence of time-averaged $\langle \beta \rangle$ and reveals a systematic increase in magnetization in going from the Twolooop-128 to the 256 zone model, but not much difference between the 256 and 512

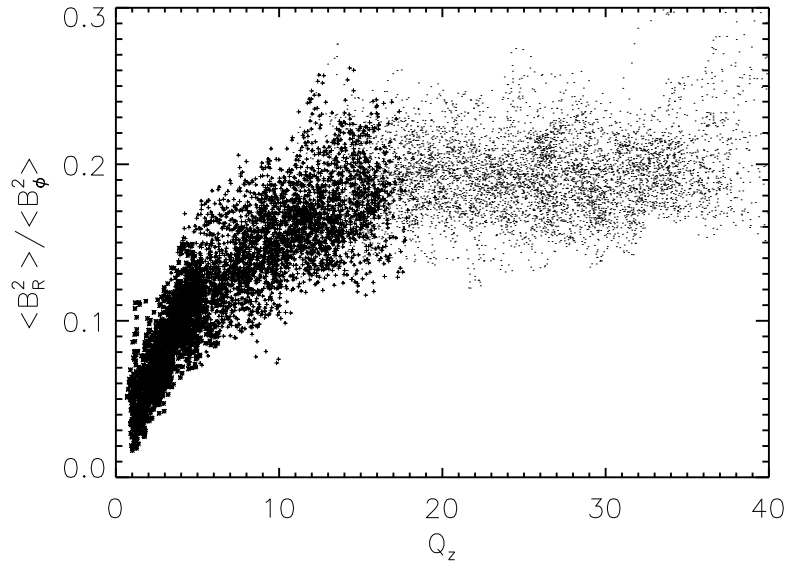


Fig. 4.— Values of $\langle B_R^2 \rangle / \langle B_\phi^2 \rangle$ versus $\langle Q_z \rangle$ for all radii between $6\text{--}20M$ and for times from $t = 4350$ to $6150M$. Stars correspond to the Twoloop-128 run, plus signs to the Twoloop-256 run, and points to the Twoloop-512 run.

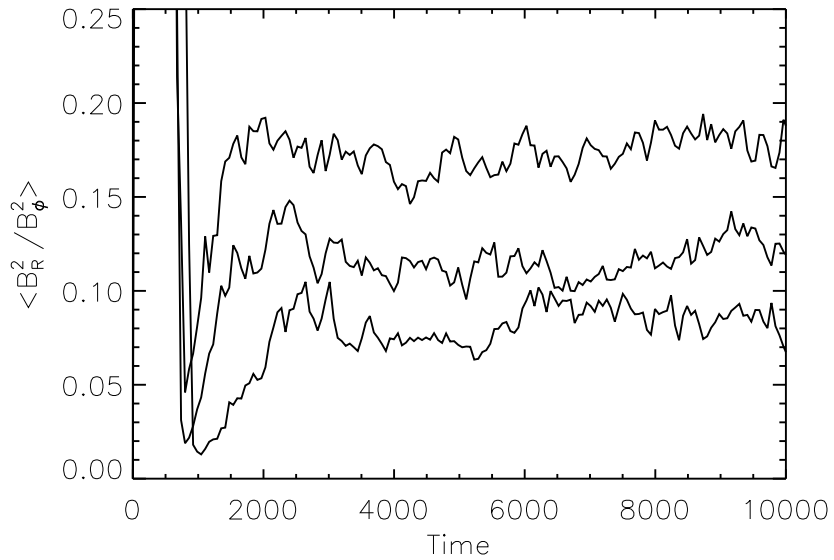


Fig. 5.— Time evolution of $\langle B_R^2 \rangle / \langle B_\phi^2 \rangle$ averaged between $R = 6$ and $20M$ for the three resolutions of the two-loop simulations. From top to bottom the curves correspond to Twoloop-512, Twoloop-256, Twoloop-128. Compare with Fig. 4 of Hawley et al. (2011).

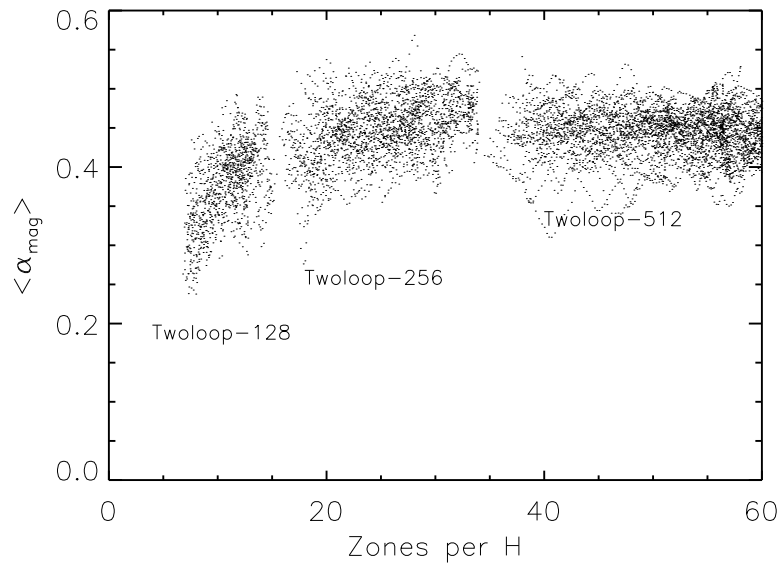


Fig. 6.— Values of α_{mag} versus number of grid zones per H for all radii between $10\text{--}20M$ and for times from $t = 4000$ to $6150M$. The three different runs inhabit distinct regions of the plot, labeled Twoloop-128, Twoloop-256 and Twoloop-512. The scatter shows the relatively wide range of variation in α_{mag} . A systematic decline is observed for resolutions less than 20 zones per H .

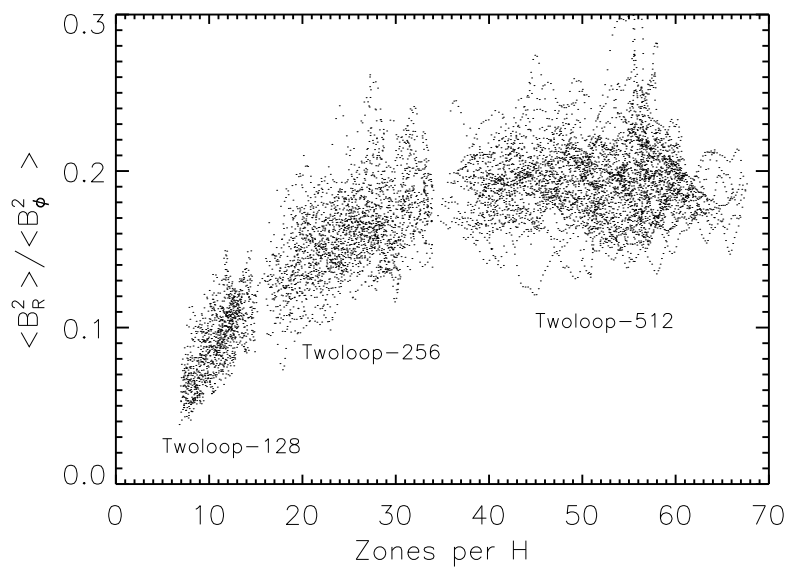


Fig. 7.— Values of $\langle B_R^2 \rangle / \langle B_\phi^2 \rangle$ versus number of grid zones per H for all radii between $10\text{--}20M$ and for times from $t = 4000$ to $6150M$. The three different runs inhabit distinct regions of the plot, labeled Twoloop-128, Twoloop-256 and Twoloop-512. The scatter shows the relatively wide range of variation in $\langle B_R^2 \rangle / \langle B_\phi^2 \rangle$. A systematic increase with resolution is observed up to approximately 35 zones per H .

models. Although the total magnetic energy changes significantly over the simulation in response to mass loss, the magnetization β shows much less variation within the inner disk. The error bars in Fig. 8 show one standard deviation in value over the averaging time for Twolooop-512.

Figure 9 is a plot of the time-averaged Shakura-Sunyaev parameter $\alpha_{SS} = \alpha_{mag}/\beta$ as a function of zones per scale height H for the Two-loop runs, from the ISCO out to $R = 20M$. (Note that this definition of α_{SS} does not include the Reynolds stress.) The advantage in plotting α_{SS} instead of the code value of the Maxwell stress is that the latter varies systematically with mass loss due the overall evolution of the disk; α_{SS} shows much less secular variation with time. Plotting against zones per scaleheight provides separation for the curves; disks that are thicker or that have higher resolution will be shifted to the right. Moving left to right along each curve corresponds to moving from smaller to larger R . The point marked with a cross on each curve corresponds to the value at $R = 10M$. In order of increasing resolution these values are $\alpha_{SS} = 0.02, 0.033, \text{ and } 0.034$. For Twolooop-512, $\alpha_{SS} \approx 0.03\text{--}0.04$ between $R = 10\text{--}20M$. α_{SS} increases sharply near the ISCO as the gas pressure falls and $M_{R\phi}$ increases. This is an example of a global effect that would not be seen in a shearing box model. Although our focus is on the properties within the main body of the disk, it is worth noting that the stress increases rapidly inside the ISCO, and this “plunging region” stress increases systematically with resolution. (Again, recall that with a cylindrical grid the number of zones per scale height decreases inward when H/R is constant.)

The next column of Table 2 gives the average disk thickness, H/R , at the ISCO and $R = 20M$. Although the initial disk had $H/R = 0.07$, it thickens considerably. Disk turbulence is sustained by the continuing action of the MRI, and the turbulent magnetic and velocity fluctuations are dissipated at the grid scale. *Athena* uses an energy conserving algorithm; numerical losses in kinetic and magnetic energy are converted into heat. The resulting increase in H improves the nominal measure of resolution quality, namely the number of z zones per H . At $t = 5474M$, for example, the three different resolutions have $H/\Delta z$, of 64, 32, and 14 zones at $R = 20M$. At the ISCO, H is smaller and the zones per scale height is reduced to 22, 10, and 4.

Finally, the last column in the Table gives the density-weighted Maxwell stress. Not surprisingly, given the zones per scale height there, the biggest relative difference between resolutions is near the ISCO.

How do the outcomes compare with the predicted zone requirements as expressed in Eqns. (5) and (6)? Using the time-averaged values for β , H/R and the components of the magnetic energy, the number of ϕ zones needed to achieve at least $\langle Q_\phi \rangle = 10$, N_ϕ , ranges from 31–50, 35–50, and 51–66 between the ISCO and $R = 20M$ for the Twolooop-512, 256

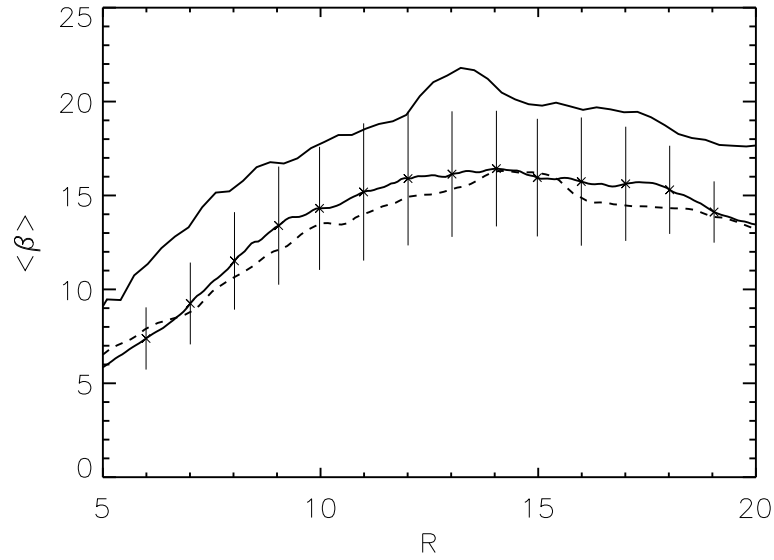


Fig. 8.— The radial dependence of time-averaged $\langle \beta \rangle$. The time average is taken between $t = 4000$ – $6150M$. The top curve corresponds to the Twoloop-128 run, the dashed curve to Twoloop-256, and the bottom solid curve to Twoloop-512. The error bars on the Twoloop-512 curve show the standard deviation of β over the time interval.

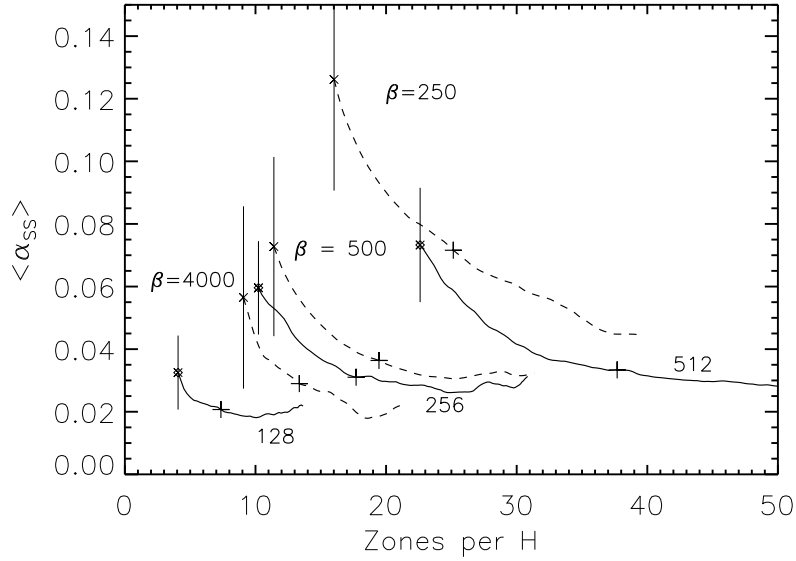


Fig. 9.— The density-weighted Maxwell stress parameter, $\alpha_{SS} = -B_R B_\phi / 4\pi P_{gas}$, time-averaged from $t = 4000$ – $6150M$, versus number of zones per time-averaged scale-height between $R = 6$ – $20M$ for several two-loop runs. The solid lines are the three resolution experiments and the dashed lines are field strength experiments labeled by the initial β value. Scale height increases with radius and, since Δz is fixed for each resolution, plotting against number of zones per H provides separation for the curves. The error bar at the end of each curve corresponds to the standard deviation of the stress over the time interval at the ISCO. The cross on each curve marks the value of α_{SS} at $R = 10M$.

and 128 models respectively. All three models are adequately resolved in ϕ by this criterion, although Twolooop-128 is only marginally so, and its value of $\langle Q_\phi \rangle$ is the lowest. The required number of vertical zones per H , N_z , is another matter, however, with computed values of 21–23, 28–24, and 57–34 for the Twolooop-512, 256 and 128 models. At the ISCO, only Twolooop-512 model meets this criterion, and Twolooop-128 doesn’t even meet it at $R = 20M$. Thus, the number of zones required to maintain adequate resolution throughout a simulation *decreases* with *increasing* initial resolution. The reason for this behavior is that simulations with better-quality initial resolution achieve stronger field strengths at saturation, whose demands on resolution are weaker, while simulations with initially poor resolution create weaker fields, requiring finer resolution to describe. As a result, only simulations that are well-resolved at the initial condition can hope to reach physical saturation levels.

In summary, there are differences between all three resolutions studied here. In the initial evolution the magnetic field grows more rapidly and to a higher amplitude with increasing resolution. The initial field strength is weak enough that the initial Q_z values are somewhat marginal for Twolooop-256, and clearly under-resolved for Twolooop-128. This is reflected in the early evolution, and the level of magnetization reached at the end of initial growth period influences what occurs subsequently. The highest resolution simulation has achieved the targeted Q values. Whether the simulation is “converged” at least in the sense that no further significant quantitative differences would be seen with higher resolution, remains uncertain, but seems likely. The plot of $\langle B_R^2 \rangle / \langle B_\phi^2 \rangle$ versus $\langle Q_z \rangle$ suggests that Twolooop-512 is adequately resolved and that $\langle B_R^2 \rangle / \langle B_\phi^2 \rangle \approx 0.2$ is the value achieved under those circumstances. By the same criteria, Twolooop-256 is nearly adequately resolved and Twolooop-128 is clearly under-resolved. This is reflected in the relative stress levels seen in the simulations. Looking at the number of grid zones per H in the simulations, the results are consistent with the shearing box conclusion that “adequate resolution” is achieved for > 32 zones per H .

Despite being demonstrably under-resolved, the Twolooop-128 model nevertheless evolves in a *qualitative* manner similar to the higher resolution models, at least initially. Low resolution simulations can be usefully employed in surveys of disk evolution scenarios, but caution is in order in assessing quantitative values, especially if confidence in the simulation is based solely on the appearance of seemingly robust accretion.

These conclusions follow from a particular problem configuration. We next consider the effects of variations on that configuration.

4. Simulation Variations

4.1. Effect of Initial Field Strength

Accretion simulations begin from an idealized initial condition usually consisting of some well-ordered magnetic field configuration. The long term evolution of the resulting flow is driven by MRI-driven turbulence that develops from this initial state. Well-resolved ideal MHD stratified shearing box simulations have found that MRI turbulence can be sustained indefinitely and that the properties of the turbulence are independent of the topology or strength of the initial field in the absence of a net B_z field through the box. (The situation is more complex for non-ideal MHD. The study of Rempel et al. (2010) shows, for example, that finite resistivity can cause zero net flux MRI-driven nonstratified shearing box turbulence to gradually decay.) Compare the recent high-resolution results from Simon et al. (2011), Davis et al. (2010), Guan & Gammie (2011) and Simon et al. (2012), for example. The key term here is “well resolved.” Turbulence either fails to develop or dies out if the initial field is too weak with respect to the resolution (i.e., low Q value), or if there is insufficient range between λ_{MRI} and the resistive scale in simulations where resistivity is included.

The *first* requirement for an adequately resolved simulation is an adequately resolved initial field as indicated by $\langle Q_z \rangle$ or $\langle Q_\phi \rangle$. To explore the effect of the initial field strength we repeat the two-loop fiducial simulation with a weaker initial field ($\beta = 4000$, Twoloop-256w), and stronger fields ($\beta = 500$, Twoloop-256l; $\beta = 250$, Twoloop-256b). The field strength is characterized in terms of β , but for the purposes of resolution considerations it is more appropriate to use $\langle Q_z \rangle$. With the two-loop field configuration, the maximum initial $\langle Q_z \rangle$ is found near the pressure maximum and is equal to 2, 4, 5.7, and 8 from the weakest to the strongest field. As previously remarked, the fiducial run is already below the standard criterion of $\langle Q_z \rangle > 6$, so the weakest field model will be at an even greater disadvantage.

Although the initial field topology is the same in all these runs, the different field strengths lead to considerable differences in the evolution. The poloidal magnetic field grows due to the MRI and all wavelengths longer than $\sim \lambda_{MRI}/\sqrt{3}$ are unstable. While these wavelengths are unstable (e.g., those on order H), the growth rate at a fixed wavelength longer than λ_{MRI} is $\propto v_A$, and hence is small for weak fields. Both these factors retard the overall field amplification and the onset of turbulence as β increases. The weakest field model, Twoloop-256w, reaches its peak poloidal field energy at $t = 4100M$. As field strength increases, the peak occurs earlier: the fiducial run peaks at $t = 3000M$, Twoloop-256l at $t = 2800M$, and Twoloop-256b at $t = 2700M$. For the toroidal field, amplification is primarily through shear acting on the radial field, $dB_\phi/dt \propto -B_R\Omega t$, hence the growth rate of B_ϕ is proportionally reduced for weaker fields.

Figure 9 plots the time-averaged α_{SS} for the Maxwell stress as a function of zones per scale height H for the two-loop runs. The $\beta = 250$ model, Twoloop-256b, has a particularly large Maxwell stress, apparently benefiting both from the larger initial field strength and the thicker disk that develops due to greater rates of heating. From weakest to strongest initial field strength, α_{SS} at $R = 10$ (marked with a cross in Fig. 9) is 0.029, 0.033, 0.036 and 0.072. Again, α_{SS} is proportional to magnetization, β^{-1} . The accretion rate as a function of mass on the grid also increases within initial field strength, consistent with the observed increase in α_{SS} .

Table 2 shows that all the quality metrics improve with increasing initial field strength. Here the greatest difference is between the weakest initial field, Twoloop-256w, and the others. The values of $\langle B_R^2 \rangle / \langle B_\phi^2 \rangle$ increase substantially, almost doubling from Twoloop-256w to Twoloop-256b. On the whole Twoloop-256w resembles Twoloop-128. The values of the initial $\langle Q_z \rangle$ in both those simulations are equivalent. This illustrates that the question of adequate resolution is not solely one of grid zones, or even of initial β . Rather the ratios between the grid zone size and the MRI wavelength—i.e., $\langle Q_z \rangle$ and $\langle Q_\phi \rangle$ —are the best indicator, not only for the initial field growth, but also for the subsequent evolution.

4.2. Effect of Numerical Algorithm

The outcome of a numerical simulation is not solely determined by the grid resolution; the numerical algorithm itself can be very significant. Algorithmic effects are particularly important for under- or marginally-resolved simulations. The optimal choice of algorithm may not be clear-cut. Kritsuk et al. (2011), for example, carried out a detailed comparison of a number of MHD codes on a particular turbulence simulation, and the results were qualitatively similar, but with some variation in details. No scheme emerged as the clear winner. Flock et al. (2010) studied the effect of numerical scheme and Riemann solver on the linear MRI in a global disk and found that the proper treatment of Alfvén characteristics in the Riemann solver is crucial.

Because *Athena* is designed with a choice of state reconstruction schemes and flux solvers, it offers an opportunity to test what a single algorithmic change has on the various physical and diagnostic quantities on the same global disk problem. By default we use the third-order piecewise-parabolic reconstruction with the HLLD flux solver. Using our fiducial run as a baseline we can compare simulations that use second-order, piecewise-linear reconstructions and the HLLD flux solver (Twoloop-256s), and a simulation with third-order reconstruction and the HLLE flux solver (Twoloop-256e). In principle, the use of second-order reconstruction will lead to larger truncation error compared to the use of third-order

reconstruction. As for the flux solvers, the HLLE scheme uses only information from the fastest wave speeds; it is diffusive for contact discontinuities. The HLLD scheme corrects this by considering the full family of wavespeeds, but at a cost of greater computational complexity. Beckwith & Stone (2011) found that HLLD was approximately 1.5 times more accurate than the HLLE solver as measured in an Alfvén wave convergence test.

A comparison with the fiducial run shows that either algorithmic change delays the initial linear growth phase and reduces the field energy growth rate. Use of the HLLE flux solver most reduces the growth rate. Table 2 also shows some decrease in the quantitative diagnostic values; a reduction in $\langle B_R^2 \rangle / \langle B_\phi^2 \rangle$ is particularly noticeable in both Twolooop-256s and Twolooop-256e. Figure 10 is the time-average value of α_{SS} as a function of zones per scale-height H in the three resolution simulations and the second-order and HLLE simulations. The value of α_{SS} at $R = 10M$ is 0.021 for the HLLE simulation, the same as Twolooop-128, and 0.034 for the second-order simulation, the same as the fiducial run. The HLLE simulation’s effective resolution is comparable with the Twolooop-128 run, while the use of second-order reconstruction has had only a minimal effect compared to the fiducial simulation. This result is not, however, universal. In §4.4 we will see that the use of second-order interpolation has a significant effect when the initial field is toroidal.

4.3. One Loop

The simulations with a two-loop initial field configuration found that both resolution and initial field strength can affect the quantitative outcome. To test the impact of initial field topology, we next consider three resolutions of an initial $\beta = 1000$ one-loop field, labeled Oneloop-512, Oneloop-256 and Oneloop-128. For the one-loop field, the vertical field is located at the front and back of the torus. With this β the peak initial $\langle Q_z \rangle$ is 2.5 for the Oneloop-256 simulation, well below the nominal threshold for adequate resolution. The initial maximum $\langle Q_z \rangle$ for Oneloop-512 is 5, comparable with the initial $\langle Q_z \rangle$ in Twolooop-256.

The evolution of a one-loop model is *qualitatively* similar to a two-loop model, and the relative effects of resolution are the same, but the one-loop models have lower overall magnetization. The poloidal field energies and accretion rates are reduced compared to the equivalently gridded two-loop models (see Table 2). The role of the toroidal field seems particularly important. The toroidal field energy increases at the same rate for all three resolutions—it grows due to shearing of the initial radial field—but the lowest resolution model has the highest peak value. This is due to a delay in the onset of turbulence caused by lower resolution, which gives the relatively unperturbed coherent radial field a longer period of shear amplification.

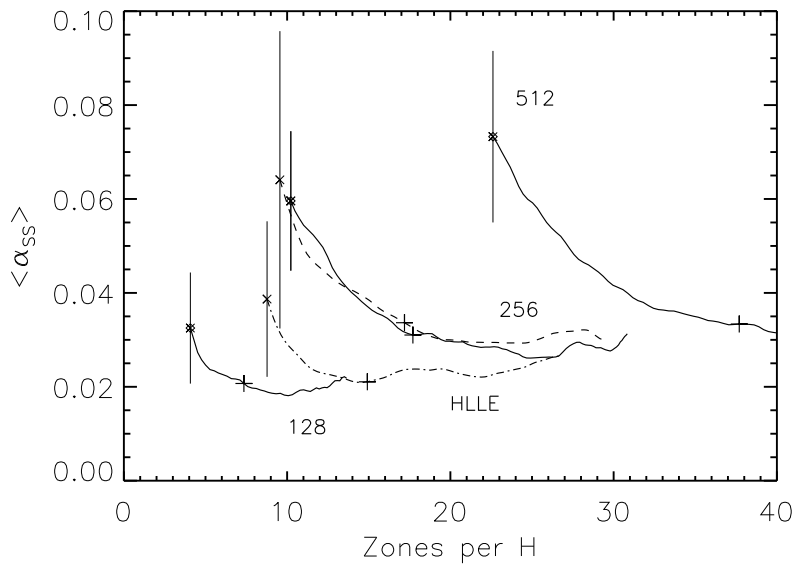


Fig. 10.— The Shakura-Sunyaev for the density-weighted Maxwell stress $\alpha_{SS} = -B_R B_\phi / 4\pi P_{gas}$ time-averaged from $t = 4000$ – $6150M$, versus number of zones per time-averaged scale-height between $R = 6$ – $20M$ for several two-loop runs. The solid lines are the three resolution experiments, the dashed line corresponds to the model run with second-order reconstruction, and the dot-dashed line is the model run with the HLLC flux solver. The error bar at the end of each curve corresponds to the standard deviation of the ISCO stress over the time interval.

In the turbulent evolution phase, the one-loop models all have stress levels that are below the lowest resolution two-loop model. The reduced stress in the one-loop models also leads to reduced heating and smaller disk scale heights relative to the two-loop models. Figure 11 plots the time averaged α_{SS} as a function of zones per H for the one-loop models. Although the stress is reduced compared to the two-loop models, within the body of the disk α_{SS} is similar for all three resolutions. For example, at $R = 10M$, $\alpha_{SS} = 0.024$, 0.024 , and 0.023 for the 128, 256 and 512 resolution models, even though the zones per H vary from 7 to 30 at that radius. Resolution has a more obvious impact near the ISCO, where the number of zones per H is 4, 9, and 19, and $\alpha_{SS} = 0.032$, 0.046 and 0.056 . If we compute N_z using equation (5) and the time-averaged values from the simulations, we find that adequate resolution would require 70, 37, 27 vertical zones at the ISCO. The largest number of zones would be required for the Oneloop-128 run because its magnetization is lower compared to the other simulations. All three are adequately resolved by the $\langle Q_\phi \rangle$ criterion. At $R = 20M$, H is larger and is spanned by 50, 22 and 11 zones, with the N_z criterion calling for 29, 39, and 34 zones per H . By both the $\langle Q_z \rangle$ and $\langle Q_\phi \rangle$ criteria the 128 and 256 models are under-resolved, and the 512 model is only marginally resolved.

Figure 12 is a plot of $\langle B_R^2 \rangle / \langle B_\phi^2 \rangle$ versus $\langle Q_z \rangle$ for all radii between $R = 6\text{--}20M$ and times $t = 4000\text{--}6150M$. While it has the same appearance as Fig. 4, as does a time history of the average value of $\langle B_R^2 \rangle / \langle B_\phi^2 \rangle$, Oneloop-512 has a mean $\langle Q_z \rangle$ of 16 and mean $\langle B_R^2 \rangle / \langle B_\phi^2 \rangle$ of 0.17, both lower than Twoloop-512 for the same time- and radius-interval.

The change in field topology from two- to one-loop, while maintaining the same average β , resulted in a reduction of magnetic field energy at a given resolution. The total magnetization in the evolved state is not due to the topology so much as it is due to the initial field strength. Although the one-loop and two-loop models have equivalent initial average β , the different topologies give different initial $\langle Q_z \rangle$; the one-loop configuration has a weaker B_z field.

To explore this further we carry out Oneloop-320b, a simulation with an average initial field strength of $\beta = 100$ and a grid with $320 \times 120 \times 256$ zones. This grid maintains Δz as in the fiducial run, sets $\Delta R = \Delta z$, and reduces $\Delta\phi$ to 0.0131. By increasing the strength of the field, the initial $\langle Q_z \rangle$ is increased to ~ 7 , making the linear vertical field modes adequately resolved. (This is the strength of the field that was used in the Hawley & Krolik (2001) simulation.) The evolution proceeds more rapidly than the $\beta = 1000$ models. The mass on the grid also drops rapidly; by $t = 6662M$ only 10.7% of the original torus mass remains. The value of α_{SS} at $R = 10M$ is 0.048, twice that for the $\beta = 1000$ one-loop models. Because of this more rapid evolution, the averaging period for the data in Table 2 is $t = 2000\text{--}4000M$.

The one-loop configuration lends itself to the production of toroidal field through shear

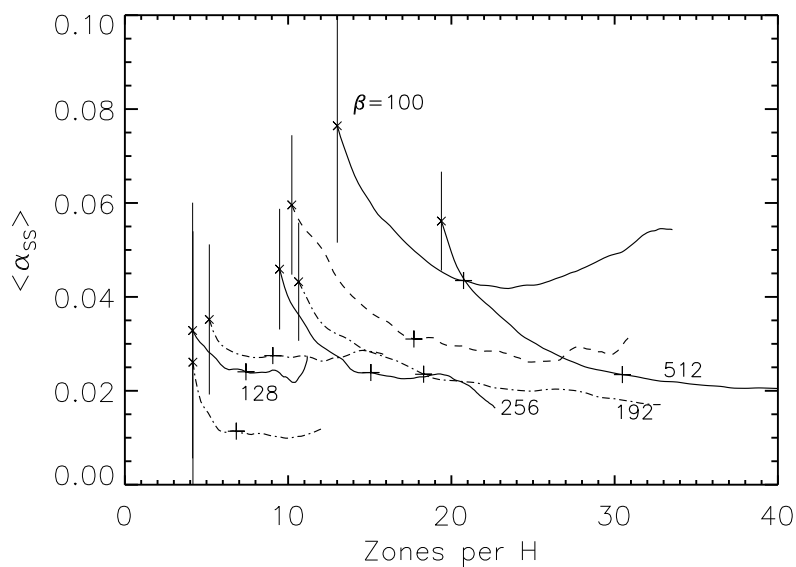


Fig. 11.— Time-averaged α_{SS} for the one-loop runs (solid lines) and the toroidal field runs Toroidal-192, -128 and -64(dot-dashed lines), as a function of zones per H . The toroidal field runs are time-averaged from $t = 10^4$ – $1.4 \times 10^4 M$. The fiducial two-loop run is include for comparison (dashed line). The point marked by a cross on each curve indicates the value of α_{SS} at $R = 10M$.

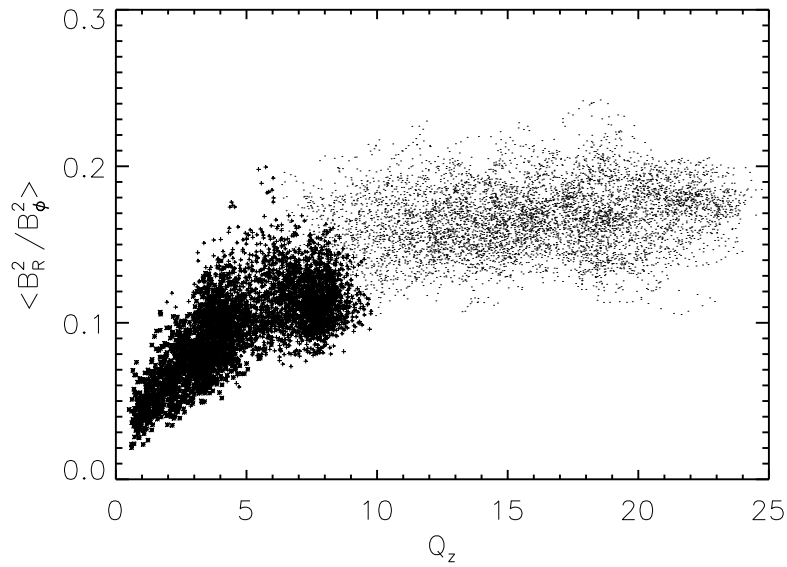


Fig. 12.— Values of $\langle B_R^2 \rangle / \langle B_\phi^2 \rangle$ versus $\langle Q_z \rangle$ for all radii between $6\text{--}20M$ and for times from $t = 4000$ to $6150M$. Stars correspond to the Oneloop-128 run, plus signs to the Oneloop-256 run, and points to the Oneloop-512 run.

acting on the initial radial field. Since Oneloop-320b has $\beta = 100$, the radial field is $10^{1/2}$ times larger than in the other one-loop models. This results in a toroidal field with $\beta < 1$ away from the equatorial plane. In that sense, Oneloop-320b is a strong toroidal field model, producing some of the largest $\langle Q_\phi \rangle$ values in all the simulations. A similar statement can be made for the disk thickness, as H/R is second to only the strongest field two-loop model. The values of $\langle Q_z \rangle$, α_{mag} and $\langle B_R^2 \rangle / \langle B_\phi^2 \rangle$ are comparable to the Oneloop-512 model, indicating again that what constitutes “adequate resolution” depends on the initial conditions. The stress is considerably larger than in all the other one-loop simulations, as seen in α_{SS} (Fig. 11).

To summarize these results, for one-loop configurations as well as for two-loop, the best indicators of long-term success in a simulation are its initial values of $\langle Q_z \rangle$ and $\langle Q_\phi \rangle$.

4.4. Toroidal Field

We next turn to the evolution of initial toroidal field configurations. A uniform toroidal field is often used in shearing box initial conditions, and is of general interest because toroidal fields dominate in an accretion disk due to the orbital shear. For example, it is likely that the $\beta = 1000$ one-loop models are controlled primarily by the toroidal field generated above and below the equatorial plane. In the earliest shearing box simulations (Hawley & Stone 1995; Hawley et al. 1995), models with net toroidal fields behaved much like those initialized without a net field. More recently, Sorathia et al. (2012) made the same observation for the cylindrical disk.

A purely toroidal weak field in a differentially rotating plasma is MRI unstable, although technically it is a transient amplification; k_r , the radial wavenumber of a given mode, evolves due to the background shear (Balbus & Hawley 1992). For a toroidal field, the unstable modes are nonaxisymmetric, and the most unstable has an azimuthal wavelength $\sim \lambda_{MRI}$. The greatest amplification occurs for large k_z , which suggests that high resolution might well be required in both the azimuthal and vertical dimensions to capture the behavior of the MRI.

Using the same domain as before, including the limited $\pi/2$ extent in ϕ , we consider three initial toroidal field simulations at different resolutions: Toroidal-64 with $128 \times 64 \times 128$ resolution, Toroidal-128 with $128 \times 128 \times 128$ resolution, and Toroidal-192 with $256 \times 128 \times 192$ resolution. The MRI wavelength, λ_{MRI} , is the distance an Alfvén wave travels in one orbit, and its size compared to the size of the orbit is $\lambda_{MRI}/2\pi R = v_A/R\Omega$, the ratio of the Alfvén to orbital speed. Since the disk is highly supersonic, and the grid zone size is $R\Delta\phi$, a

relatively strong initial magnetic field is required if $\langle Q_\phi \rangle$ is to be large enough in the main body of the disk. Here we use a uniform toroidal field with $\beta = 10$, defined in terms of average gas pressure to average magnetic pressure. Because the Alfvén speed varies in the torus, the initial $\langle Q_\phi \rangle$ also varies from ~ 7 – 13 from the center to the outer radial edge of the torus using the 64-zone grid; $\langle Q_\phi \rangle$ is doubled for the 128-zone grid. We also consider a model with a $\beta = 100$ initial field strength (Toroidal-128w), for which $\langle Q_\phi \rangle = 5$ – 7 initially for the 128-zone ϕ grid. And finally, we ran a $\beta = 10$ model using second-order interpolation (Toroidal-128s).

Toroidal field initial conditions have a longer initial MRI growth phase before fully developed turbulence sets in. This is obvious in a plot of the time-history of the poloidal field energy (Fig. 13). The growth rates for the poloidal field energy (which begins at zero) are highly dependent on the details of the simulation. Improved R and z resolution (Toroidal-192) increases the initial growth rate of the poloidal field components, but does not significantly alter the peak total energies in the turbulent state compared to Toroidal-128. Cutting the azimuthal resolution in half (Toroidal-64) decreases both the growth rate and the peak energy.

Because of the delay in the onset of turbulence, the diagnostic values for the $\beta = 10$ experiments (Table 2) are time-averaged from $t = 1.0$ – $1.4 \times 10^4 M$. In the case of the $\beta = 100$ initial toroidal field model, turbulence developed at a very late time, and the time-average is taken from $t = 3.0$ – $4.0 \times 10^4 M$. The quality factor $\langle Q_z \rangle$ is quite generally smaller for the toroidal field models than for those that begin with a poloidal field. The $\langle Q_\phi \rangle$ values, on the other hand, are comparable or larger. The resolution in R and z seems to matter less than that of the ϕ direction. When accounting for the change in Δz , the $\langle Q_z \rangle$ values for Toroidal-192 and Toroidal-128 are comparable, but the reduction to only 64 azimuthal zone reduces $\langle Q_z \rangle$ well below the minimum of ~ 6 . Similarly $\langle Q_\phi \rangle$ is lower by more than a factor of two in Toroidal-64. Only Toroidal-192 has an α_{mag} in the range associated with adequate resolution. The same can be said for $\langle B_R^2 \rangle / \langle B_\phi^2 \rangle$, except that even for Toroidal-192 the maximum value is below 0.2 associated with the best-resolved models. Plotting $\langle B_R^2 \rangle / \langle B_\phi^2 \rangle$ versus $\langle Q_z \rangle$ as was done in Fig. 4 (not shown) again finds a correlation between the two. For Toroidal-192 $\langle B_R^2 \rangle / \langle B_\phi^2 \rangle$ flattens out at ~ 0.15 as a function of $\langle Q_z \rangle$; $\langle Q_z \rangle$ does not exceed ~ 15 .

How do these results translate into effective stress? Figure 11 shows time-averaged α_{SS} for the three $\beta = 10$ toroidal field runs, time-averaged from $t = 1.0$ – $1.4 \times 10^4 M$. The curves for Toroidal-192 and Toroidal-128 are similar to the $\beta = 1000$ one-loop models, with $\alpha_{SS} = 0.024$ and 0.027 respectively at $R = 10M$. Toroidal-64 has a significantly lower value of $\alpha_{SS} = 0.011$.

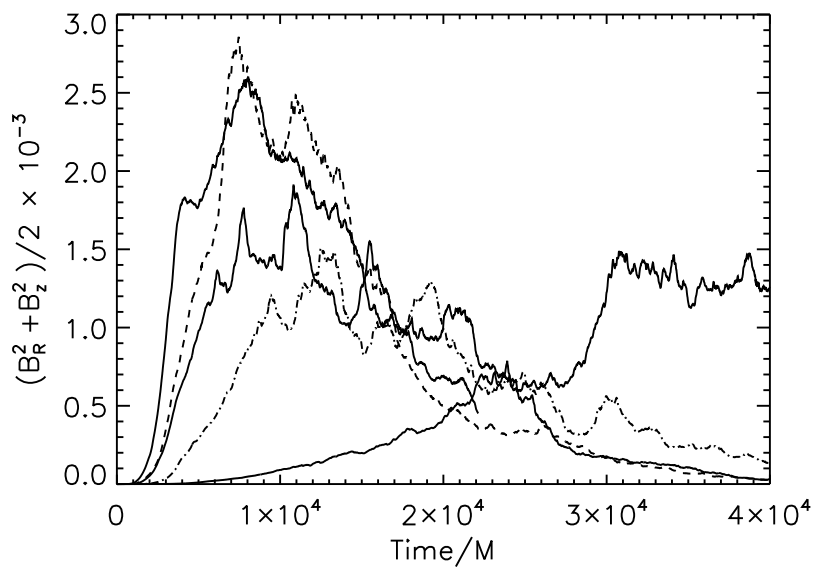


Fig. 13.— Time-evolution of the total poloidal magnetic field energy for the initial toroidal field models. From left to right the first solid curve is Toroidal-192, the dashed curve is Toroidal-128, the next solid curve is Toroidal-64, the dot-dashed line is Toroidal-128s, which uses second-order interpolation, and the last curve is Toroidal-128w, which began with a $\beta = 100$ strength field and only achieves a turbulent state for $t > 3.0 \times 10^4 M$.

The difference between Toroidal-128 and Toroidal-64 indicates that (not surprisingly) azimuthal resolution is critical. This is re-enforced by the experiment where the interpolation scheme is reduced to second-order (Toroidal-128s). Unlike the case with the (better-resolved) two-loop configuration, where the use of second-order had relatively little apparent effect, here it produces a significant reduction in growth rate and peak energy, even compared to Toroidal-64 which has half the azimuthal zones. The orbital velocity is aligned with the initial magnetic field, and nonaxisymmetric perturbations experience numerical diffusion that works against the MRI. The resulting values for α_{mag} , $\langle B_R^2 \rangle / \langle B_\phi^2 \rangle$, and $Q_{z,\phi}$ are comparable to those of Toroidal-64 (Table 2). The use of second-order interpolation reduces the initial MRI growth rates, and the subsequent turbulent state is affected. Twoloop-256s appeared unaffected by second-order interpolation, but it was twice as well resolved in R and z as Toroidal-128s. Well-developed MRI-driven turbulence relies on robust generation of poloidal field, and the increase of diffusion error in the toroidal direction is compounded by the low poloidal resolution. The resulting value of $\langle B_R^2 \rangle / \langle B_\phi^2 \rangle$ demonstrates this.

Toroidal-128w has an initial field strength of $\beta = 100$ and, as such, has a significantly reduced initial $\langle Q_\phi \rangle$. Figure 13 shows that while there is still field amplification, it is at a greatly reduced rate. Wavelengths longer than λ_{MRI} are still unstable, i.e., those with low azimuthal wavenumber m , but at growth rates that are reduced $\propto \lambda^{-1}$ compared to the maximum rate. During this initial phase, the MRI grows fastest at the edges of the torus, where the density is low and the Alfvén speed is larger compared to the interior. It takes until $t = 3 \times 10^4 M$ for significant field growth to occur in the core of the disk. Accretion begins only beyond this point in time. The total poloidal field energy at late time is comparable to that seen in Toroidal-64 (Fig. 13) near its maximum. The data in Table 2, time-averaged within this period, reflect a level of magnetization that is consistent with the Toroidal-64 model. A reduction in initial field strength is comparable to a reduction in resolution.

Figure 14 examines the behavior of α_{mag} in these simulations as a function of zones Δz per scale height. The data are individual density-weighted averages at all radii between $R = 10\text{--}20M$, and all times between $t = 10^4$ and $2 \times 10^4 M$. The relationship is striking: α_{mag} is reasonably constant for (roughly) 15 zones per H and drops off, at a very rapid rate for zone number less than 10. The labeled horizontal lines indicate the minimum and maximum zone numbers and minimum α_{mag} for the simulation. The time interval corresponds to when the Toroidal-128w run has not yet achieved turbulence throughout its interior, and it has the lowest α_{mag} values as well as the smallest number of zones per H .

Figure 15 plots $\langle B_R^2 \rangle / \langle B_\phi^2 \rangle$ against the number of zones per H in the toroidal field runs, over the same radial span and the same time period. This shows an even stronger dependence on resolution than α_{mag} . $\langle B_R^2 \rangle / \langle B_\phi^2 \rangle$ remains below 0.2, but is still increasing as

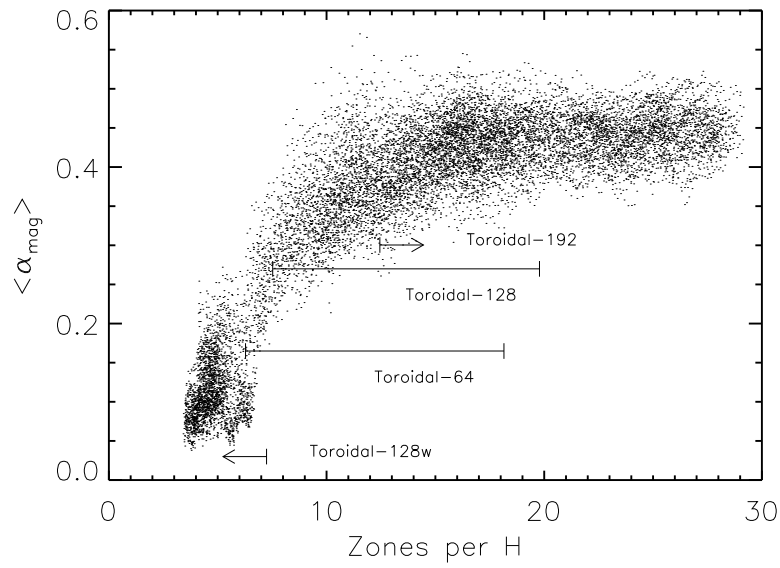


Fig. 14.— Values of α_{mag} versus number of grid zones per H for all radii between $10\text{--}20M$ and for times from $t = 1\text{--}2 \times 10^4 M$ for the initial toroidal field runs. The lines show the range of scale height and the minimum α_{mag} values for the specific run as labeled. The scatter shows the range of variation in α_{mag} . A systematic decline is observed for resolutions less than 20 zones per H .

the resolution approaches 30 zones per H .

One notable feature of initial toroidal field global simulations (Beckwith et al. 2011; Flock et al. 2012) and shearing box simulations (Simon et al. 2011) is the rapidity with which the net toroidal field disappears. For example, Figure 16 of Simon et al. (2011) shows the time-evolution of the average toroidal field in shearing box simulations compared to a similar calculation for a subdomain from a global simulation of Beckwith et al. (2011). Within approximately 10 orbits the initial net field is lost and is replaced by a net field of the opposite polarity and of comparable amplitude to the original net field. The process then reverses in an apparent cycle. This behavior is seen in shearing box space-time diagrams in (t, z) for field integrated over (x, y) , e.g., Figure 15 in Simon et al. (2012). Guan & Gammie (2011) and Simon et al. (2011) examined the time evolution of the mean field in shearing box simulations and found that it was well described by a generalized α - Ω dynamo model. The dynamo seen in local simulations also occurs within the global disk. O’Neill et al. (2011) also report seeing dynamo action in their global simulations, noting that the sign of the net toroidal field alternates on a time comparable to 10 local orbits. We also see this behavior in these simulations. In Toroidal-192, for example, we examined the time-evolution of B_ϕ integrated over a subdomain within the initial torus centered on $R = 15M$, extending from $R = 14$ – $16M$, and for $|z| < 5M$. The initial net field reverses within this subdomain within 10 orbits. While there is some indication of periodicity, it is not as regular as seen in the shearing box. This is not surprising as the shearing box is, in contrast to a global disk, characterized by a single frequency Ω .

In sum, much the same resolution criteria hold for simulations with initially toroidal magnetic field as for those with initially poloidal field. If the simulation is to result in fully-developed MHD turbulence, the initial (and continuing) quality factors must be large enough: $\langle Q_z \rangle \gtrsim 15$ and $\langle Q_\phi \rangle \gtrsim 20$. These can be achieved by different combinations of initial β and grid resolution, but these criteria must be met one way or another.

4.5. Transients versus Turbulence

The simulations presented throughout this paper compare the outcomes using different resolutions and numerical algorithms, but all runs within a comparison group begin from a specific idealized, non-turbulent initial condition. As a consequence they all experience a linear growth phase for the MRI followed by the onset of turbulence and the development of quasi-steady state accretion that lasts until the matter supplied by the initial condition is depleted. The properties of the resulting turbulence might depend on the way the initial linear growth period, with all its transient effects, depends on resolution. To what extent

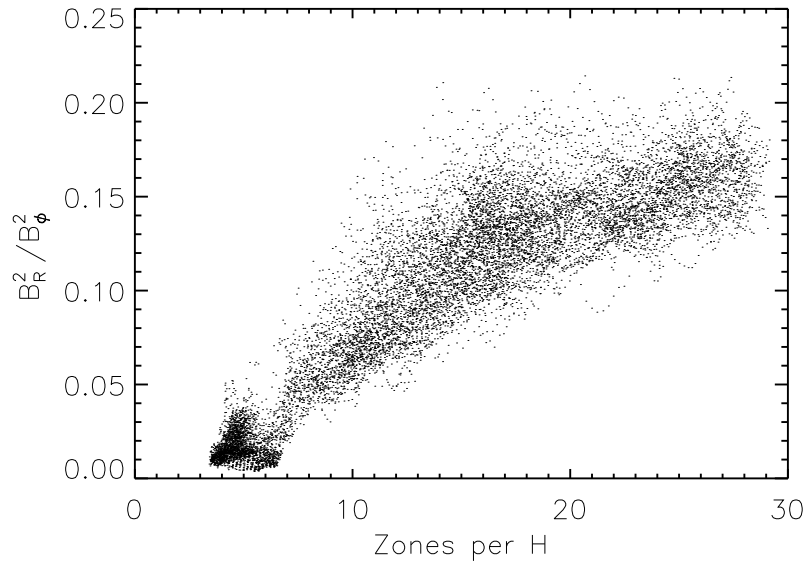


Fig. 15.— Values of $\langle B_R^2 \rangle / \langle B_\phi^2 \rangle$ versus number of grid zones per H for all radii between $10\text{--}20M$ and for times from $t = 1\text{--}2 \times 10^4 M$ for the initial toroidal field runs. The scatter shows the range of variation in $\langle B_R^2 \rangle / \langle B_\phi^2 \rangle$ which systematically increases as zones per H increase.

are the reduced turbulent and magnetic energies seen at low resolution due to how the simulation emerges from the start-up phase, and to what extent is it due to a given resolution’s inadequacy in resolving the turbulent phase itself?

Of course, most simulations start from an idealized, and relatively simple, initial condition, with all the associated initial transient effects, so this study is representative of the typical case. But, it is possible to investigate more directly the influence of resolution on the turbulent state itself by performing an experiment in which the quasi-steady state disk is the initial condition. We start with run a high resolution, $512 \times 128 \times 512$, simulation that begins with the fiducial two-loop initial condition. This is labeled “Twoloop-512t” (for turbulent) and is evolved well into the quasi-steady state phase. At time $t = 4600M$ the data from this simulation are copied onto successively coarser grids of $256 \times 64 \times 256$ (Twoloop-256t) and $128 \times 32 \times 128$ (Twoloop-128t). All three resolutions are then evolved forward and compared.

To re-grid the data to lower resolution, we use an *Athena* restart file corresponding to time $t = 4600M$. The fundamental data in an *Athena* zone are volume-averaged values of density, momentum and total energy, and face-centered magnetic fluxes. The volume element for a grid zone is $RdRdzd\phi$. To go from a fine grid to a coarser grid we do a volume-weighted average over the zones that make up the single larger zone on the coarser grid. This conserves total mass and momentum in the re-grid process. The magnetic field, on the other hand, is area-averaged over those zone faces that make up the new larger zone face. This preserves net flux and the divergence-free property of the magnetic field on the new grid. The regrid process results in some loss of magnetic energy as oppositely directed fields undergo numerical reconnection. The total loss in magnetic energy is 7.2% in Twoloop-256t, and 23% in Twoloop-128t. Thus, re-gridding introduces by itself a change that will produce a transient response in the simulation. Similarly, some kinetic energy is lost by the volume average onto the new grid. Kinetic energy is dominated by the orbital component, which barely changes, but the poloidal kinetic energy decreases by 2% and 8% respectively. Because of the loss of magnetic and kinetic energy, we choose to regrid the internal energy and reconstruct the new total energy on the coarse grid. This avoids an abrupt change in disk temperature due to thermalization of the interpolation losses as the simulation is restarted.

After restart, the coarse grid simulations relax to a new quasi-steady state with reduced magnetic energy. This is rapid, occurring within only $50M$, showing that it is a local phenomenon as numerical dissipation occurs at the new, coarse grid resolution. We consider the interval between $t = 5040$ – $6030M$, a point in time after the re-gridded runs have re-established a quasi-steady state. Figure 16 shows the time-averaged vertically integrated poloidal magnetic field energy as a function of radius. The coarser grids simply cannot sustain as high a magnetization, a conclusion that follows without regard to the evolution

history.

This is reflected in the diagnostic values, which are listed in Table 2. Again these are time-averaged between $t = 5040\text{--}6030M$. Comparison of these diagnostic values with the values in similarly resolved grids run from the initial state (Twolooop-256 and Twolooop-128) show great similarity. Again, because the simulations relax to this state on a relatively short time, it seems that the observed level of turbulence is simply what a given resolution can support.

Figure 17 plots the value of $\langle B_R^2 \rangle / \langle B_\phi^2 \rangle$ versus zones per scale height H for these three simulations. It should be compared with Fig. 7. The distribution of points is similar in the two plots, although here the disks are modestly thicker and the points are shifted to higher numbers of zones per H compared to Fig. 7. This is a difference from the equivalently resolved models that were run from the initial condition: the thicker disk should give make up somewhat for low resolution. However, the overall behavior of the $\langle B_R^2 \rangle / \langle B_\phi^2 \rangle$ diagnostic with effective resolution remains the same. Small scales are important in fully developed MRI-driven turbulence, and the quality parameters, Q , provide a measure of a grid’s ability to resolve those features adequately.

5. Conclusions

One of the most important scientific goals of global accretion disk simulations is the ability to make detailed observational predictions from first-principles physics. Although the thermodynamics employed in global simulations remains primitive and other important dynamical elements like radiation forces have yet to be implemented outside shearing-box models, in recent years several groups have initiated programs to use the bolometric energy budgets of simulations for this purpose (Noble et al. 2011; Kulkarni et al. 2011; Zhu et al. 2012; Schnittman & Noble 2012) The quantitative quality of these predictions depends, of course, on the quality of the simulation data underlying them. Any parameter inferences (e.g., the black hole spin parameter) will be subject to a systematic error traceable to deficiencies in the resolution data.

In this paper, we have attempted to clarify the computational and numerical limitations associated with global simulations at the limits of resolution achievable with contemporary computational resources. We have found that resolution and numerical algorithm, as well as initial field strength and topology, can affect the quantitative values of MRI-driven accretion in global simulations. Considerable care is needed to sort through these effects when interpreting simulation outcomes.

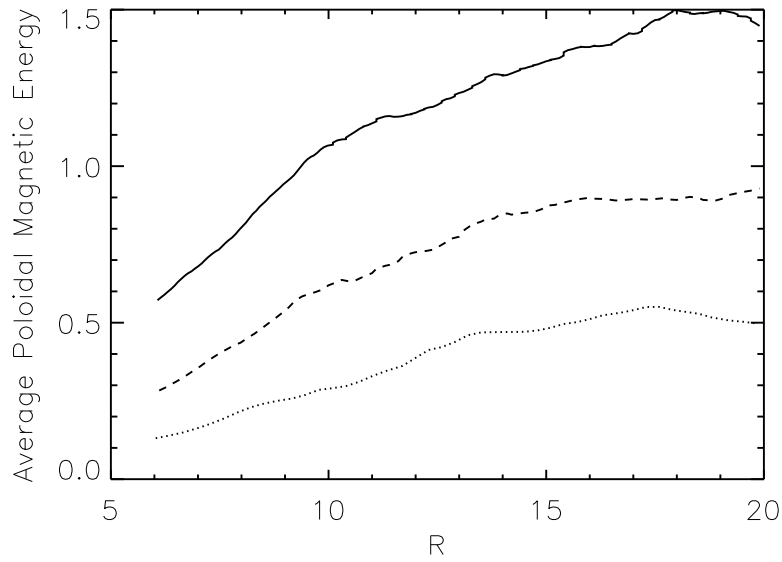


Fig. 16.— The vertically integrated poloidal magnetic field energy ($\times 10^4$) as a function of radius between 6–20 M time-averaged from $t = 5040$ to 6640 M for the turbulent restart test runs. The solid line is Twoloop-512t, the dashed line Twoloop-256t, and the dotted line is Twoloop-128t.

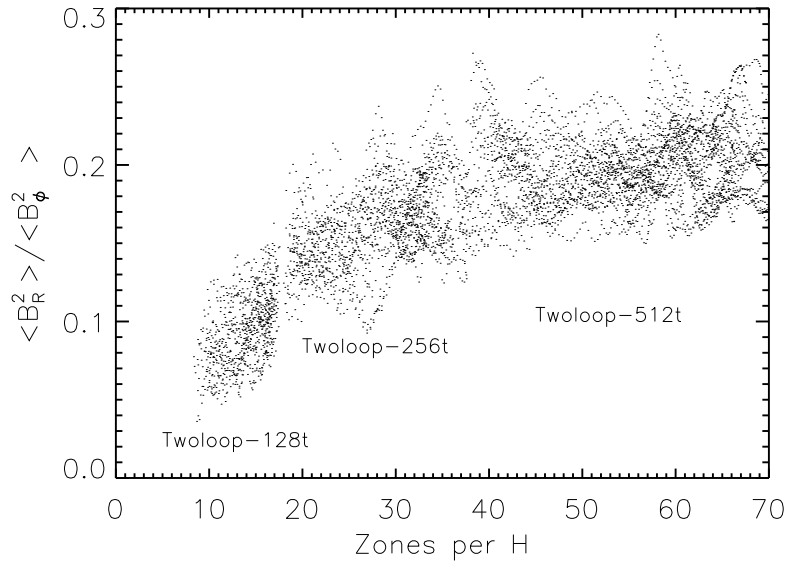


Fig. 17.— Values of $\langle B_R^2 \rangle / \langle B_\phi^2 \rangle$ versus number of grid zones per H for all radii between $10\text{--}20M$ and for times from $t = 5040$ to $6640M$ for the turbulent restart test runs. The three different runs inhabit distinct regions of the plot, labeled Twoloop-128t, Twoloop-256t and Twoloop-512t. The scatter shows the relatively wide range of variation in $\langle B_R^2 \rangle / \langle B_\phi^2 \rangle$.

In particular, the quality factors $\langle Q_z \rangle$ and $\langle Q_\phi \rangle$ are valuable measures of resolution, for both the initial conditions and in the fully developed MRI-driven turbulence. Low Q values are unambiguous markers of inadequate resolution and, consequently, uncertain quantitative values. Low resolution leads to reduced stress, incompletely developed turbulence, and reduced accretion rates, but not necessarily a complete cessation of accretion. However, when the resolution is especially coarse or there is an especially large downward fluctuation in the magnetic intensity, the turbulence may die altogether. Shiokawa et al. (2012) carried out a convergence study of a general relativistic accretion simulation and observed just this behavior in their lowest resolution simulation consisting of $96 \times 96 \times 64$ zones in (r, θ, ϕ) .

By contrast, high Q values indicate adequate resolution. Moreover, because adequate resolution leads to larger magnetic saturation levels, sufficiently high Q values in the initial state can lead to still higher values as the simulation proceeds. The key question we have attempted to answer is, of course, how to define the threshold of “adequacy”, beyond which there are only insignificant changes in the simulation. Hawley et al. (2011) estimated minimum values of $\langle Q_z \rangle \geq 10$ and $\langle Q_\phi \rangle \geq 20$. These values were incorporated into (5) and (6) to estimate the required number of grid zones for a simulation. In this paper we found that these equations provide a reasonable estimate of the number of zones needed for adequate resolution. A modest increase in the target $\langle Q_z \rangle$ and $\langle Q_\phi \rangle$ would probably provide a better estimate. Figure 4 suggests $\langle Q_z \rangle \geq 15$, for example. This is broadly consistent with the results of Shiokawa et al. (2012), who argued that their highest resolution simulation, at $384 \times 384 \times 256$ zones, was nearly adequately resolved; it featured Q values equivalent to $\langle Q_\phi \rangle \sim 22$ and $\langle Q_z \rangle \sim 9$ – 29 in the near hole region.

The threshold values of the two quality factors are not independent of each other; higher $\langle Q_\phi \rangle$ values can compensate for low $\langle Q_z \rangle$. Sorathia et al. (2012) suggest that $\langle Q_z \rangle > 10$ – 15 is required for $\langle Q_\phi \rangle \approx 10$, and that $\langle Q_\phi \rangle > 25$ compensates for low $\langle Q_z \rangle$. The latter conjecture is supported by our toroidal field runs where $\langle Q_z \rangle$ was clearly low, but with $\langle Q_\phi \rangle \sim 30$ turbulence was nevertheless sustained with good α_{mag} and $\langle B_R^2 \rangle / \langle B_\phi^2 \rangle$ values. We did not have an example with a large $\langle Q_z \rangle$ and a low $\langle Q_\phi \rangle$; we did not perform any simulations with a net vertical field and a low ϕ grid count, the most likely scenario where that could be observed.

The present simulations also provided considerable data with which to test the behaviors of two other simulation quality indicators describing the physical character of the turbulence rather than the resolution, α_{mag} (which has the equivalent information as the tilt angle used in other studies), and the ratio of radial to toroidal magnetic field energy, $\langle B_R^2 \rangle / \langle B_\phi^2 \rangle$. Although these two diagnostics are related, they are not equal. The tilt-angle, or α_{mag} , is the “efficiency” of a field configuration by measuring the degree of correlation between B_r

and B_ϕ , whereas $\langle B_R^2 \rangle / \langle B_\phi^2 \rangle$ measures the ability of the turbulence to generate poloidal field, through the MRI-dynamo process. We find that $\alpha_{mag} < 0.4$ indicates inadequate resolution. There is a relation between α_{mag} and the number of grid zones per vertical scale height; above 20 zones per H , α_{mag} levels off at around 0.45 which corresponds to a magnetic tilt angle of 13° . $\langle B_R^2 \rangle / \langle B_\phi^2 \rangle$ also shows a dependence with resolution, but one that is more demanding than seen with α_{mag} . $\langle B_R^2 \rangle / \langle B_\phi^2 \rangle$ levels off at ≈ 0.2 in the best resolved case when $H/\Delta z \geq 35$. This is consistent with the consensus emerging from local simulations that adequate resolution requires greater than 32 zones per H . Finally we note that both $\langle B_R^2 \rangle / \langle B_\phi^2 \rangle$ and α_{mag} are proportional to $\langle Q_z \rangle$ until they reach their limiting values.

Based on these criteria, of the simulations we have done for this paper, excluding the numerical algorithm tests, only the Twolooop-512, Twolooop-512t, and Twolooop-256b simulations are adequately resolved, and the later is resolved by virtue of its relatively strong initial magnetic field. Twolooop-256, Twolooop-256l, Onelooop-512, Onelooop-320b, and Toroidal-192 are marginally resolved and the other simulations are under-resolved to varying degrees. Because our criteria are similar to those of Hawley et al. (2011), we support their judgment of which published thin disk simulations are close to adequate resolution: only the set reported by Noble et al. (2010) meet the test; because the vertical cell size in the simulations of Penna et al. (2010) are $\simeq 4\times$ larger, it is likely that they fall short.

In accretion disks the R - ϕ stress is of fundamental importance, and stress levels can be affected by resolution. The time-averaged α_{SS} values in the adequately resolved $\beta = 1000$ two-loop simulations are $\alpha_{SS} = 0.030$ – 0.035 , out in the main body of the disk from $R = 10$ – $20M$. These values are consistent with shearing box results (e.g. Simon et al. 2012) with the caveat that the α values reported for shearing boxes typically include the Reynolds as well as the Maxwell stress. For the under-resolved simulations, however, $\alpha_{SS} = 0.02$ – 0.029 .

Stress can be increased in the models by using stronger initial fields. Twolooop-256b has an initial $\beta = 250$ and has a time-averaged $\alpha_{SS} = 0.072$ at $R = 10M$; Onelooop-320b, with an initial $\beta = 100$ has $\alpha_{SS} = 0.048$. An increase in stress with initial field has also been seen in shearing boxes that have net fields (Hawley & Stone 1995).

Although our focus in this paper is on the stress in the main part of the disk, we do observe significant non-zero stress near the ISCO, and these ISCO stresses are particularly sensitive to resolution. For example, the time-averaged α_{SS} at the ISCO are 0.034, 0.065 and 0.076 for the 128, 256 and 512 resolution two-loop $\beta = 1000$ simulations (see Fig. 9). Under-resolved simulations can significantly under-value the near-ISCO stresses compared to simulations that are adequately resolved in terms of the quality metrics.

In considering the stress levels found in these simulations, one should bear in mind that

we are considering the *numerical* convergence for a particular physical model, here inviscid, ideal MHD without radiation physics. Simulations that use a different physical model could get α_{SS} values that are different from those found here. Regardless of the physical model used, however, one should demonstrate that the resolution used in a given simulation is sufficient so that stress levels are no longer significantly changed by increasing resolution.

While the number of zones per scaleheight in the disk is an important metric, the strength of the (initial) magnetic field is also important. Here Q provides valuable guidance as a better way to characterize the initial field than some initial averaged β . If Q is small initially, the MRI will have difficulty establishing itself and sustaining a steady state. Any reduced turbulence in the initial evolution carries over to the turbulent evolution of the disk. This effect is amplified where heating occurs. Stronger MRI turbulence leads to stronger heating, increasing the scale height H , and hence the number of zones per scaleheight. The simulations that were adequately resolved initially became more so as a consequence of their evolution.

The effect of resolution on the level of magnetization and turbulence in the quasi-steady state is intrinsic; reduced turbulence levels are not solely the result of a failure to properly resolve the initial linear MRI. When we take a well-resolved turbulent disk and remap it onto lower resolution grids, the magnetic energy rapidly readjusts to new, lower level. Coarser grids cannot sustain as high a level of magnetization, regardless of the evolution history.

We have found that adequately resolved global simulations have α_{SS} values that are consistent with shearing box simulations that use the same physics. We also found another important similarity between global and local models: global simulations demonstrate clear evidence of dynamo behavior as observed in the shearing box. This agrees with O’Neill et al. (2011) who observed dynamo behavior in their global simulations. The dynamo is less coherent than seen in shearing boxes, however. Global simulations lack any special orbital frequency, unlike the shearing box, and experience secular evolution with time.

Although MRI-driven turbulence in global simulations is very similar to turbulence in a shearing box, there are specific effects discernible only with a global treatment. One of the most obvious is the change with radius of disk properties, notably including the consistent sharp rise in stress toward the ISCO when there is adequate resolution. As discussed by Sorathia et al. (2012) global models differ from local models in a fundamental way due to the secular evolution of the former, at least for global simulations to date. The timescale for the secular evolution of the disk is much shorter than the timescale for the establishment of steady state MHD turbulence. The initial evolution in shearing box simulations lasts at least 10 orbits, and characteristic values are usually derived from boxes that have been run for times greater than 50 orbits. In this sense, not only do global disks tend to be under-resolved

relative to shearing boxes, they also tend to be under-evolved. This represents a significant challenge, both in total grid size and in evolution time. Even though one can run hundreds of orbits at the ISCO, the inner disk must be fed from an outer disk that evolves on a much longer timescale. A long term steady state in an inner accretion disk requires that it be fed at a steady rate from large radius in a self-consistent manner and for a significant number of orbits.

Looking forward, it appears that adequate resolution can be achieved in global simulations, but it requires a considerable number of zones. Because computational resources are always finite, they must be placed adroitly in order to have the most positive impact on the quality of the simulation. We recommend:

- When the disk aspect ratio H/R is constant, spherical coordinates are best, as they allow one to maintain a constant number of zones per H , independent of R . If instead the disk scale height H is constant, cylindrical coordinates would be preferable for the same reason.
- Use of the HLLD flux solver rather than a diffusive solver like HLLE. The use of a higher-order reconstruction scheme can be important for improved results, particularly at marginal resolution.
- The initial conditions of any simulation must be well-resolved as indicated by $\langle Q_z \rangle$ and $\langle Q_\phi \rangle$.
- Adequate resolution in both the poloidal and azimuthal directions is essential. In terms of the quality factors we have defined, this means $\langle Q_z \rangle \gtrsim 10\text{--}15$ and $\langle Q_\phi \rangle \gtrsim 20$, although an especially high value in one of the Q parameters can compensate for a slightly low value in the other. These values must be maintained at adequate levels throughout the simulation; this goal can generally be achieved when there are at least $\simeq 35$ vertical cells per scale height in the disk body. All these criteria apply to all the magnetic topologies we have examined so far: single poloidal loops, dual poloidal loops, and purely toroidal initial field.

Acknowledgements

This work was partially supported by NASA grant NNX09AD14G and NSF grant AST-0908869 (JFH) and NSF grant AST-0908336 (JHK). Some of the simulations described here were carried out on the Kraken system at NICS, supported by the NSF. We thank Jake

Simon for comments on this work. We thank the referee for suggesting the regrid tests described in §4.5.

REFERENCES

- Balbus, S. A. & Hawley, J. F. 1991, *ApJ*, 376, 214
- . 1992, *ApJ*, 400, 610
- . 1998, *Reviews of Modern Physics*, 70, 1
- Beckwith, K., Armitage, P. J., & Simon, J. B. 2011, *MNRAS*, 416, 361
- Beckwith, K. & Stone, J. M. 2011, *ApJS*, 193, 6
- Blackman, E. G., Penna, R. F., & Varnière, P. 2008, *New Astronomy*, 13, 244
- Colella, P. 1990, *J. Comp. Phys.*, 87, 171
- Colella, P. & Woodward, P. 1984, *J. Comp. Phys.*, 54, 174
- Davis, S. W., Stone, J. M., & Pessah, M. E. 2010, *ApJ*, 713, 51
- Flock, M., Dzyurkevich, N., Klahr, H., & Mignone, A. 2010, *A&A*, 516, A26
- Flock, M., Dzyurkevich, N., Klahr, H., Turner, N., & Henning, T. 2012, *ApJ*, 744, 144
- Fromang, S. & Nelson, R. P. 2006, *A&A*, 457, 343
- Fromang, S., Papaloizou, J., Lesur, G., & Heinemann, T. 2007, *A & A*, 476, 1123
- Guan, X. & Gammie, C. F. 2009, *ApJ*, 697, 1901
- . 2011, *ApJ*, 728, 130
- Hawley, J. F. 2000, *ApJ*, 528, 462
- Hawley, J. F., Gammie, C. F., & Balbus, S. A. 1995, *ApJ*, 440, 742
- Hawley, J. F., Guan, X., & Krolik, J. H. 2011, *ApJ*, in press
- Hawley, J. F. & Krolik, J. H. 2001, *ApJ*, 548, 348
- Hawley, J. F. & Stone, J. M. 1995, *Computer Physics Communications*, 89, 127

- Kritsuk, A. G., Nordlund, A., Collins, D., Padoan, P., Norman, M. L., Abel, T., Banerjee, R., Federrath, C., Flock, M., Lee, D., Li, P. S., Mueller, W.-C., Teyssier, R., Ustyugov, S. D., Vogel, C., & Xu, H. 2011, ArXiv e-prints
- Kulkarni, A. K., Penna, R. F., Shcherbakov, R. V., Steiner, J. F., Narayan, R., Sä Dowski, A., Zhu, Y., McClintock, J. E., Davis, S. W., & McKinney, J. C. 2011, MNRAS, 414, 1183
- Lesur, G. & Longaretti, P. 2007, MNRAS, 378, 1471
- Miyoshi, T. & Kusano, K. 2005, JCP, 208, 315
- Noble, S. C., Krolik, J. H., & Hawley, J. F. 2010, ApJ, 711, 959
- Noble, S. C., Krolik, J. H., Schnittman, J. D., & Hawley, J. F. 2011, ApJ, 743, 115
- O’Neill, S. M., Reynolds, C. S., Miller, M. C., & Sorathia, K. A. 2011, ApJ, 736, 107
- Penna, R. F., McKinney, J. C., Narayan, R., Tchekhovskoy, A., Shafee, R., & McClintock, J. E. 2010, MNRAS, 408, 752
- Rempel, E. L., Lesur, G., & Proctor, M. R. E. 2010, Physical Review Letters, 105, 044501
- Sano, T., Inutsuka, S., Turner, N. J., & Stone, J. M. 2004, ApJ, 605, 321
- Schnittman, J. D. Krolik, J. H. & Noble, S. C. 2012, ArXiv e-prints
- Shafee, R., McKinney, J. C., Narayan, R., Tchekhovskoy, A., Gammie, C. F., & McClintock, J. E. 2008, ApJ, 687, L25
- Shakura, N. I. & Sunyaev, R. A. 1973, A & A, 24, 337
- Shiokawa, H., Dolence, J. C., Gammie, C. F., & Noble, S. C. 2012, ApJ, 744, 187
- Simon, J. B., Beckwith, K., & Armitage, P. J. 2012, MNRAS, 2808
- Simon, J. B. & Hawley, J. F. 2009, ApJ, 707, 833
- Simon, J. B., Hawley, J. F., & Beckwith, K. 2011, ApJ, 730, 94
- Skinner, M. A. & Ostriker, E. C. 2010, ApJS, 188, 290
- Sorathia, K. A., Reynolds, C. S., Stone, J. M., & Beckwith, K. 2012, ApJ, 749, 189
- Stone, J. M., Gardiner, T. A., Teuben, P., Hawley, J. F., & Simon, J. B. 2008, ApJS, 178, 137

Zhu, Y., Davis, S. W., Narayan, R., Kulkarni, A. K., Penna, R. F., & McClintock, J. E.
2012, MNRAS, 3392